

Neuronal timescales are functionally dynamic and shaped by cortical microarchitecture

Richard Gao^{1*}, Ruud L. van den Brink⁵, Thomas Pfeffer⁶, Bradley Voytek¹⁻⁴

¹Department of Cognitive Science, ²Halıcıoğlu Data Science Institute, ³Neurosciences Graduate Program, ⁴Kavli Institute for Brain and Mind, University of California, San Diego, La Jolla, CA, USA 92093. ⁵Department of Neurophysiology and Pathophysiology, University Medical Center Hamburg-Eppendorf, Hamburg, Germany. ⁶Center for Brain and Cognition, Computational Neuroscience Group, Universitat Pompeu Fabra, 08018 Barcelona, Spain.

*e-mail: r.dg.gao@gmail.com

Data availability

All data analyzed in this manuscript are from open data sources. All code used for all analyses and plots are publicly available on GitHub at <https://github.com/rdgao/field-echos> and https://github.com/rudyvdbrink/surface_projection. See Extended Data Table 1 and 2.

Acknowledgements Support: Natural Sciences and Engineering Research Council of Canada (NSERC PGS-D) and Katzin Prize (to R.G.). Alexander Von Humboldt Foundation fellowship for post-doctoral researchers (to R.L.v.d.B). Deutsche Forschungsgemeinschaft (DFG) SFB936/A7/Z3 (to Tobias H. Donner). Sloan Research Fellowship (FG-2015-66057), the Whitehall Foundation (2017-12-73), the National Science Foundation under grant BCS-1736028, the NIH National Institute of General Medical Sciences grant R01GM134363-01, a UC San Diego, Shiley-Marcos Alzheimer's Disease Research Center (ADRC): Research Training in Alzheimer's Disease grant, and a Halıcıoğlu Data Science Institute Fellowship (to B.V.).

Author contributions R.G. and B.V. conception and electrophysiological data analysis. R.G. simulations, anatomical, and gene expression analysis. R.v.d.B and T.P. data preprocessing and conception of anatomical and gene expression analysis. R.G. wrote the manuscript with B.V. All authors edited the manuscript.

Competing interests the authors declare no competing interests.

Abstract

Complex cognitive functions such as working memory and decision-making require the maintenance of information over many timescales, from transient sensory stimuli to long-term contextual cues¹. However, while theoretical accounts predict that a corresponding hierarchy of neuronal timescales likely emerges as a result of graded variations in recurrent synaptic excitation²⁻⁴, direct evidence in the human cortex is lacking. This limits our ability to study how other cytoarchitectural and cell-intrinsic features shape the temporal patterns of cortical activity⁵⁻⁷, and whether neuronal timescales are dynamic and relevant for human cognition. Here, we use a novel computational approach to infer neuronal timescales from intracranial recordings and construct a continuous gradient across the human cortex. We find that timescales increase along the principal sensorimotor-to-association axis⁷⁻⁹, where higher-order association areas have longer neuronal timescales. These measurements reflect transmembrane current fluctuations and scale with single-unit spiking timescales across the macaque cortex¹⁰. Cortex-wide transcriptomic analysis¹¹⁻¹³ in humans confirms direct alignment between timescales and expression of excitation- and inhibition-related genes, but further identifies genes specifically related to voltage-gated transmembrane ion transporters. Finally, neuronal timescales are functionally dynamic: prefrontal cortex timescales expand during working memory maintenance and predict individual performance, while cortex-wide timescales compress with aging. Thus, neuronal timescales follow cytoarchitectonic gradients across the human cortex, and are relevant for cognition in both short- and long-terms, bridging microcircuit physiology with macroscale dynamics and behavior.

Human brain regions are broadly specialized for different aspects of behavior and cognition. For example, primary sensory neurons are tightly coupled to changes in the environment, firing rapidly to the onset and removal of a stimulus, and showing characteristically short intrinsic timescales^{14,15}. In contrast, neurons in cortical association (or transmodal) regions, such as the prefrontal cortex (PFC), can sustain their activity for many seconds when a person is engaged in working memory¹⁶, decision-making¹⁷, and hierarchical reasoning¹⁸. This persistent activity in the absence of immediate sensory stimuli reflects longer neuronal timescales, which is thought to result from neural attractor states^{19,20} shaped by NMDA-mediated recurrent excitation and fast feedback inhibition^{21,22}, with contributions from other synaptic and cell-intrinsic properties^{5,6}.

Recent studies have shown that variations in many such microarchitectural features follow continuous and coinciding gradients along a sensory-to-association axis across the cortex, including cortical thickness, cell density, and distribution of excitatory and inhibitory neurons^{2,7,8}. In particular, grey matter myelination²³, which indexes anatomical hierarchy, varies with the expression of numerous genes related to microcircuit function, such as NMDA receptor and inhibitory cell-type marker genes¹². Functionally, specialization of the human cortex, as well as structural and functional connectivity²⁴, also follow similar macroscopic gradients. In addition to the broad differentiation between sensory and association cortices, there is evidence for a finer hierarchical organization within the frontal cortex¹⁸. For example, the anterior-most parts of the PFC are responsible for long timescale goal-planning behavior^{25,26}, while healthy aging is associated with a shift in these gradients such that older adults become more reliant on higher-level association regions to compensate for altered lower-level cortical functioning²⁷.

Despite convergent observations of continuous cortical gradients in structural features and cognitive specialization, there is no direct evidence for a similar gradient of neuronal timescales across the human cortex. Such a gradient of neuronal dynamics is predicted to be a natural consequence of macroscopic variations in synaptic connectivity and microarchitectural features^{2,4,8}, and would be a primary candidate for how functional specialization emerges as a result of hierarchical temporal processing¹. Single-unit recordings in rodents and non-human primates hint at a hierarchy of timescales that increase, or expand, progressively along a posterior-to-anterior axis^{10,15,28}, while intracranial recordings and functional neuroimaging data collected during perceptual and cognitive tasks suggest likewise in humans²⁹⁻³². However, these data are either sparsely sampled across the cortex or do not measure neuronal activity at the cellular and synaptic level directly, prohibiting the full construction of an electrophysiological timescale gradient across the human cortex. As a result, while whole-cortex data of transcriptomic and anatomical variations exist, we cannot take advantage of them to dissect the contributions of synaptic, cellular, and circuit connectivity in shaping fast neuronal timescales, nor ask whether regional timescales are dynamic and relevant for human cognition (Fig. 1a).

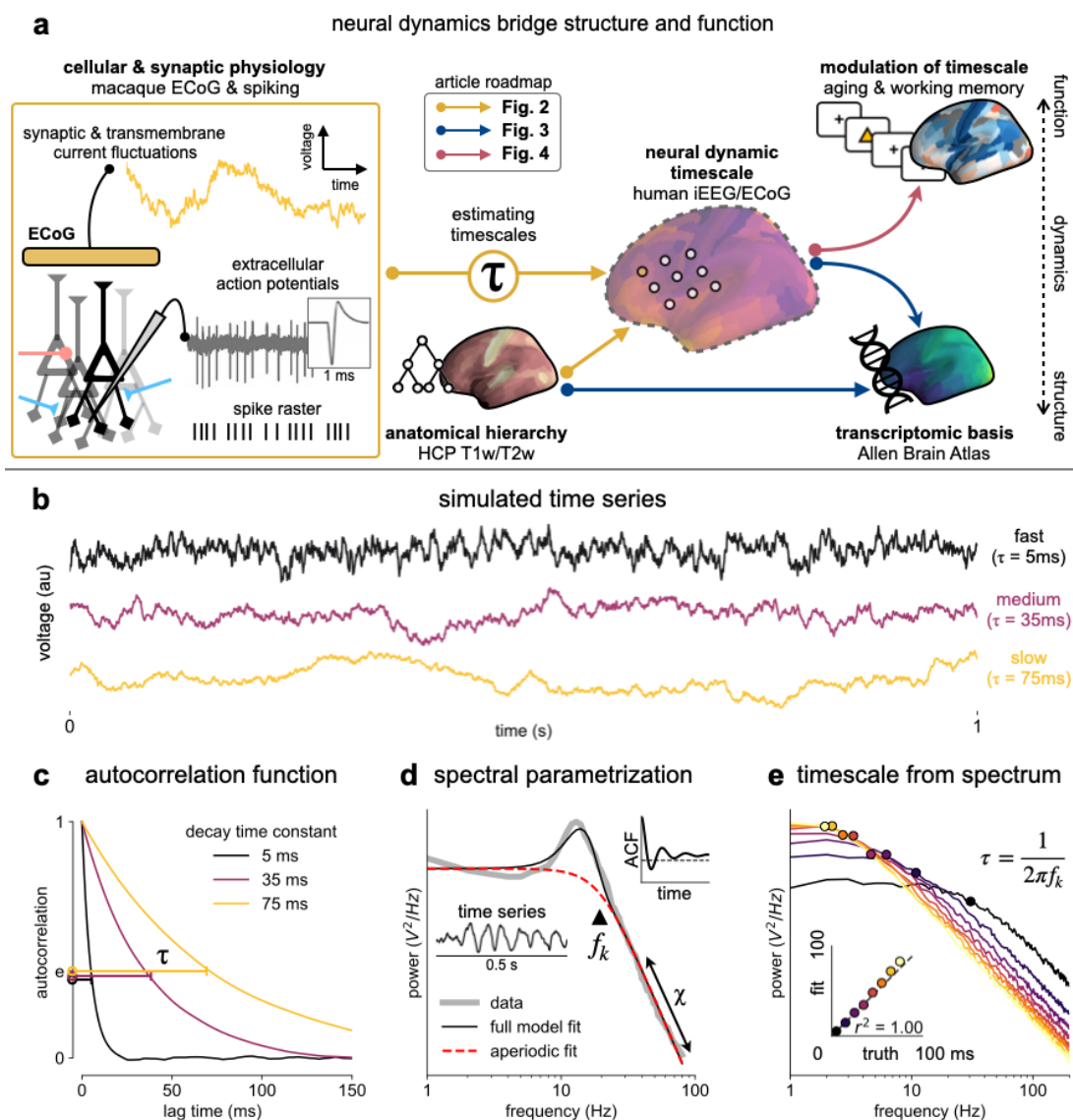


Fig. 1| Schematic of study and timescale inference technique. **a**, in this study, we infer neuronal timescales from intracranial field potential recordings, which reflect integrated synaptic and transmembrane current fluctuations over large neural populations³³. Combining multiple open-access datasets (see Extended Data Table 1), we link timescales to known human anatomical hierarchy, dissect its cellular and physiological basis via transcriptomic analysis, and demonstrate its functional modulation during behavior and through aging. **b-e**, method validation via simulation: simulated time series (**b**) with increasing timescales (defined as the decay time constant of the autocorrelation function, ACF, **c**). **d**, example macaque ECoG power spectral density (PSD) showing that in frequency domain, timescale is equivalent to the frequency of aperiodic power drop-off (f_k , triangle; insets: time series and ACF). **e**, accurate extraction of timescale parameters from PSDs of simulated time series in **b**.

Inferring neuronal timescale

To overcome these limitations, we develop a novel computational method for inferring the timescale of neuronal transmembrane current fluctuations from human intracranial electrocorticography (ECoG) recordings (Fig. 1a, box). Neural time series exhibit variable temporal autocorrelation, or timescales, where future values are partially predictable from past values, and predictability decreases with increasing time lags. To demonstrate the effect of varying autocorrelation, we simulate the aperiodic (non-rhythmic) component of neural field potential recordings by convolving Poisson population spikes with exponentially-decaying synaptic kernels (Fig. 1b). Consistent with previous studies, “neuronal timescale” here is defined as the exponential decay time constant (τ) of the autocorrelation function (ACF)¹⁰—the time it takes for the ACF to decrease by a factor of e (Fig. 1c). Equivalently, we can estimate neuronal timescale from the “characteristic frequency” (f_k) of the power spectral density (PSD), especially when the presence of variable $1/f$ (χ) and oscillatory components can bias timescale inference from the ACF in time-domain (Fig. 1d). In this study, we apply spectral parameterization³⁴ to extract timescales from intracranial recordings, which decomposes neural PSDs into a combination of oscillatory and aperiodic components, where timescale is inferred from the latter. We validate this approach on PSDs computed from simulated neural time series and show that the model-fitted timescales closely match their ground-truth values (Fig. 1e).

Timescales follow anatomical hierarchy

Applying this technique, we infer a continuous gradient of neuronal timescales across the human cortex and examine its relationship with anatomical hierarchy. We analyze a large dataset of human intracranial (ECoG) recordings of task-free brain activity from 106 epilepsy patients (MNI-iEEG³⁵, see Extended Data Fig. 1 for electrode coverage), and compare the ECoG-derived timescale gradient to the average T1w/T2w map from the Human Connectome Project, which captures grey matter myelination and indexes the proportion of feedforward vs. feedback connections between cortical regions, defining an anatomical hierarchy^{12,23}.

Across the human cortex, timescales of fast electrophysiological dynamics (~10-50 ms) predominantly follow a rostrocaudal gradient (Fig. 2a). Consistent with numerous accounts of a principal cortical axis spanning from primary sensory to association regions^{2,7,24}, timescales are shorter in sensorimotor and early visual areas, and longer in association regions, especially posterior parietal, ventral/medial frontal, and medial temporal cortex. Cortical timescales are negatively correlated with T1w/T2w ($\rho = -0.47$, $p < 0.001$; adjusted for spatial autocorrelation, see Methods and Extended Data Fig. 2), such that timescales are shorter in more heavily myelinated (lower-level) cortical regions (Fig. 2b).

While surface ECoG recordings offer much broader spatial coverage than extracellular single-unit recordings, they are fundamentally different signals: ECoG and field potentials largely reflect integrated synaptic and other transmembrane currents across many neuronal and glial cells, rather than putative action potentials from single neurons³³ (Fig. 1a, box). Considering this, we ask whether timescales measured from ECoG are related to single-unit spiking timescales along the cortical hierarchy. To test this, we extract neuronal timescales from task-free ECoG recordings in macaques and compare them to a separate dataset of single-unit

spiking timescales¹⁰ (Fig. 2c, inset; see Extended Data Fig. 3 for electrode locations). Consistent with spiking timescale estimates^{10,28}, ECoG timescales also increase along the macaque cortical hierarchy. While there is a strong correspondence between spiking and ECoG timescales (Fig. 2c; $\rho = 0.96$, $p < 0.001$)—measured from independent datasets—across the macaque cortex, ECoG-derived timescales are 10 times faster than single-unit timescales and are conserved across individual sessions (Fig. 2d). This suggests that neuronal spiking and transmembrane currents have distinct but related timescales of fluctuations, and that both are hierarchically organized along the primate cortex.

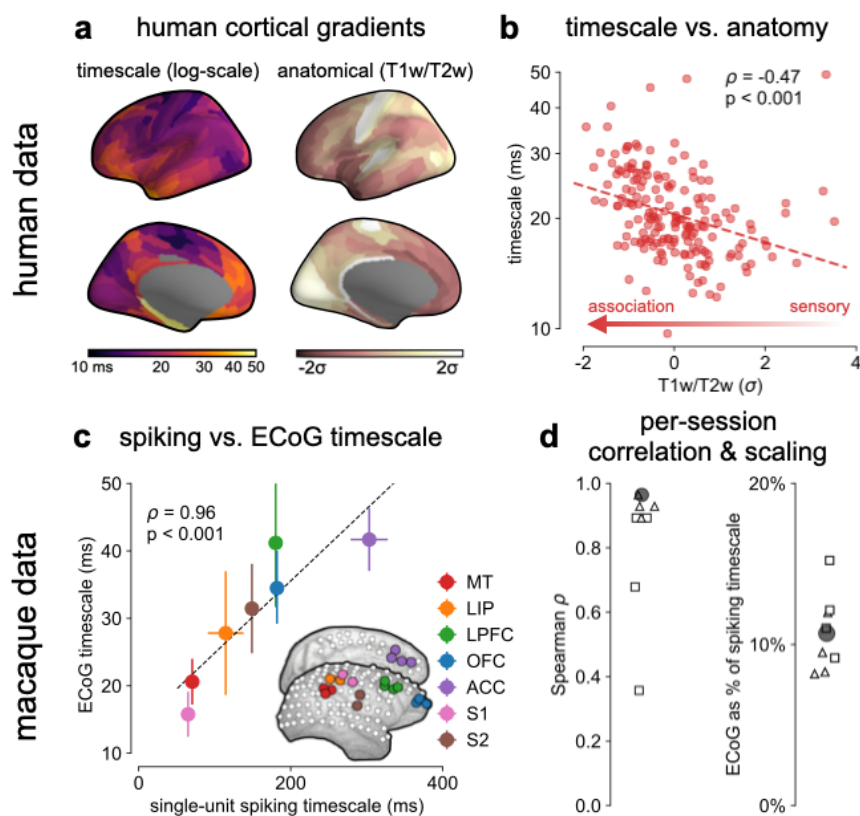


Fig. 2| Timescale increases along the anatomical hierarchy in humans and macaques. a, human cortical timescale gradient (left) falls predominantly along the rostrocaudal axis, similar to T1w/T2w ratio (right). **b**, neuronal timescales are negatively correlated with cortical T1w/T2w, thus increasing along the anatomical hierarchy from sensory to association regions (p-value adjusted for spatial autocorrelation). **c**, macaque ECoG timescales track published single-unit spiking timescales¹⁰ in corresponding regions (mean \pm s.e.m from n=8 sessions); inset: ECoG electrode map of one animal. **d**, ECoG-derived timescales are consistently correlated to (left), and an order of magnitude faster than (right), single-unit timescales across individual sessions. Hollow markers: individual sessions; shapes: animals; solid circles: grand average from **c**.

Transcriptomic basis of neuronal dynamics

Next, we identify cellular and synaptic mechanisms underlying timescale variations across the human cortex. Theoretical accounts posit that NMDA-mediated recurrent excitation coupled with fast inhibition^{4,21,22}, as well as cell-intrinsic properties^{5,6,36}, are crucial for shaping neuronal timescales. While *in vitro* and *in vivo* studies in model organisms^{37,38} can test these hypotheses at the single-neuron level, causal manipulation and large-scale recording of neuronal networks embedded in the human brain is severely limited. Here, we apply an approach analogous to multimodal single-cell profiling³⁹ and examine the transcriptomic basis of neuronal dynamics at the macroscale.

Leveraging cortex-wide bulk mRNA expression variations¹¹, we find that the neuronal timescale gradient overlaps with the dominant axis of gene expression across the human cortex ($\rho = -0.60$, $p < 0.001$; Fig. 3a and Extended Data Fig. 4). Consistent with theoretical predictions (Fig. 3b), timescales significantly correlate with the expression of genes encoding for NMDA (GRIN2B) and GABA-A (GABRA3) receptor subunits, voltage-gated sodium (SCN1A) and potassium (KCNA3) ion channel subunits, as well as inhibitory cell-type markers (parvalbumin, PVALB), and genes previously identified to be associated with single-neuron membrane time constants (PRR5)³⁹.

More specifically, *in vitro* electrophysiological studies have shown that, for example, increased expression of receptor subunit 2B extends the NMDA current time course⁴⁰, while 2A expression shortens it⁴¹. Similarly, the GABA-A receptor time constant lengthens with increasing $\alpha 3:\alpha 1$ subunit ratio⁴². We show that these relationships are recapitulated at the macroscale, where neuronal timescales positively correlate with GRIN2B and GABRA3 expression, and negatively correlate with GRIN2A and GABRA1. These results demonstrate that timescales of neural dynamics depend on specific receptor subunit combinations with different (de)activation timescales^{3,6}, in addition to broad excitation-inhibition interactions^{2,20,43}. Notably, almost all genes related to voltage-gated sodium and potassium ion channel alpha-subunits—the main functional subunits—are correlated with timescale, while all inhibitory cell-type markers except parvalbumin have strong positive associations with timescale (Fig. 3c, Extended Data Fig. 5).

We further test whether single-cell timescale-transcriptomic associations are captured at the macroscale as follows: for a given gene, we can measure how strongly its expression correlates with membrane time constant parameters at the single-cell level using patch-clamp and RNA sequencing (scRNASeq) data^{39,44}. Analogously, we can measure its macroscopic transcriptomic-timescale correlation using the cortical gradients above. Comparing across these two levels for all previously-identified timescale-related genes^{39,44}, we find a significant correlation between the strength of association at the single-cell and macroscale levels ($\rho = 0.36$ and 0.25 , $p < 0.001$ for both studies; Fig. 3d, horizontal lines). Furthermore, genes with stronger associations to timescale tend to conserve this relationship across single-cell and macroscale levels (Fig. 3d, separated by macroscale correlation magnitude). Thus, the association between cellular variations in gene expression and cell-intrinsic temporal dynamics is captured at the macroscale, even though scRNAseq and microarray data represent entirely different measurements of gene expression.

While we have shown associations between cortical timescales and genes suspected to influence neuronal dynamics, these data present an opportunity to discover additional novel genes that are functionally related to timescales through a data-driven approach. However, since transcriptomic variation and anatomical hierarchy overlap along a shared macroscopic gradient^{8,12,24}, we cannot specify the role certain genes play based on their level of association with timescale alone: gene expression differences across the cortex first result in cell-type and connectivity differences, sculpting the hierarchical organization of cortical anatomy. Consequently, anatomy and cell-intrinsic properties jointly shape neuronal dynamics through connectivity differences^{4,45} and expression of ion transport proteins with variable activation timescales, respectively. Therefore, we ask whether variation in gene expression still accounts for variation in timescale beyond the principal structural gradient, and if associated genes have known functional roles in biological processes (schematic in Fig. 4e). To do this, we first remove the contribution of anatomical hierarchy by regressing out the T1w/T2w gradient from both timescale and individual gene expression gradients. We then fit partial least squares (PLS) models to simultaneously estimate regression weights for all genes⁴⁶, submitting those with significant associations for gene ontology enrichment analysis (GOEA)⁴⁷.

We find that genes highly associated with neuronal timescales are preferentially related to transmembrane ion transporter complexes, as well as GABAergic synapses and chloride channels (Fig. 4f, Extended Data Table 3). When restricted to positively-associated genes only (expression increases with timescales), one functional group related to phosphatidate phosphatase activity is uncovered, including the gene *PLPPR1*, which has been linked to neuronal plasticity⁴⁸. Conversely, genes that are negatively associated with timescale are related to numerous groups involved in the construction and functioning of transmembrane transporters and voltage-gated ion channels, especially potassium and other inorganic cation transporters. The discovery of these gene ontology items suggests that inhibition⁴⁹—mediated by GABA and chloride channels—and voltage-gated potassium channels have prominent roles in shaping neuronal timescale dynamics at the macroscale level, beyond what's expected based on the anatomical hierarchy alone.

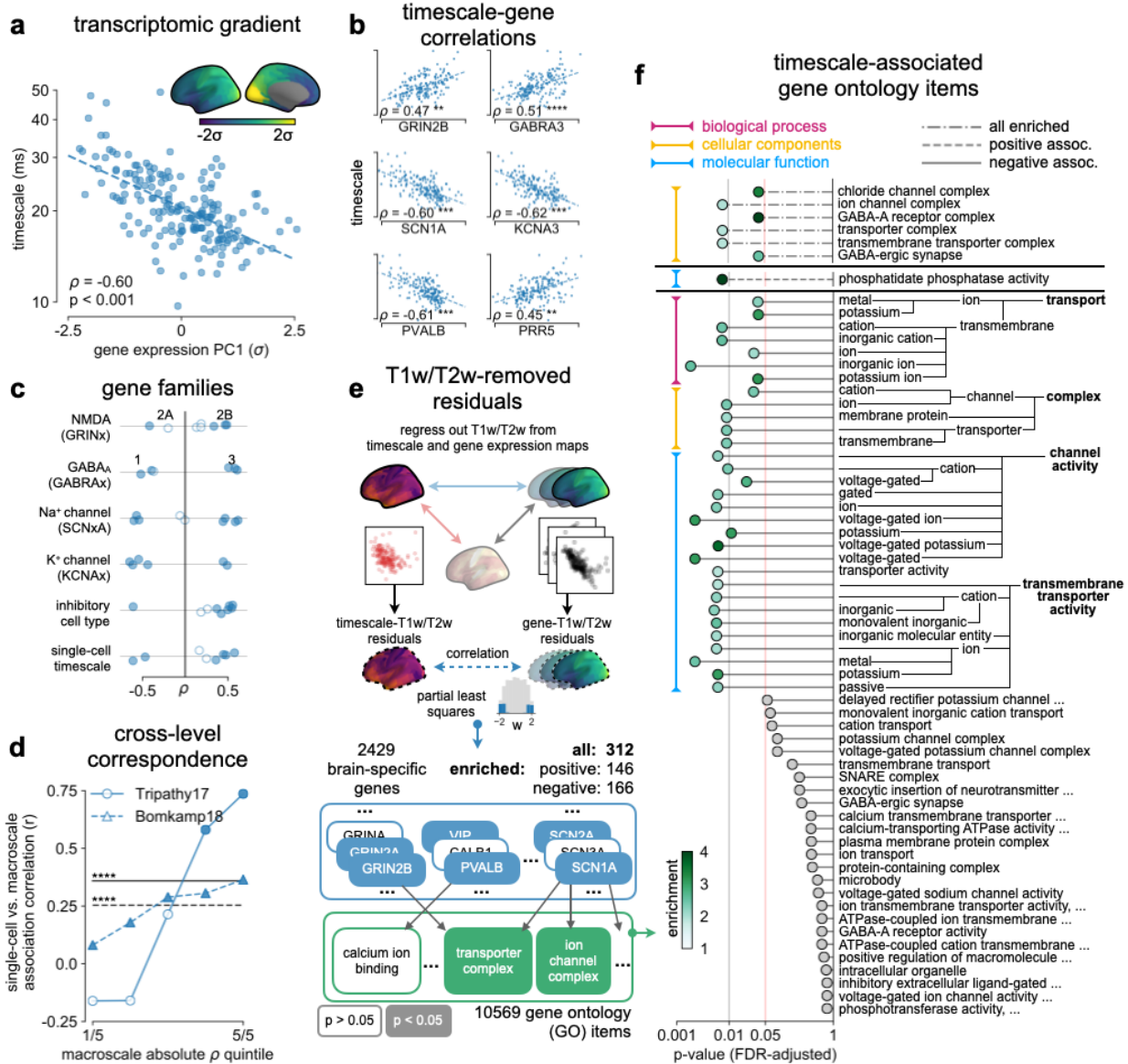


Fig. 3| Timescale gradient is linked to expression of genes related to synaptic receptors and transmembrane ion channels across the human cortex. **a**, The timescale gradient follows the dominant axis of gene expression variation across the cortex (PC1, arbitrary direction). **b-c**, timescale gradient is significantly correlated with expression of genes known to alter synaptic and neuronal membrane time constants, as well as inhibitory cell-type markers, but members within a gene family (e.g., NMDA receptor subunits) can be both positively and negatively associated with timescales (**c**). **d**, macroscale timescale-transcriptomic correlation captures association between RNA-sequenced expression of the same genes and single-cell timescale properties fit to patch clamp data^{39,44}, and the correspondence improves for genes (separated by quintiles) that are more strongly correlated with timescale (horizontal lines: correlation across all genes from ref^{39,44}, $\rho = 0.36$ and 0.25). **e**, T1w/T2w gradient is regressed out from timescale and gene expression gradients, and a partial least squares (PLS) model is fit to the residual maps. Genes with significant PLS weights are submitted for gene ontology enrichment analysis. **f**, enriched genes are primarily linked to transmembrane transporters and GABA-ergic

synapses; genes specifically with strong negative associations further over-represent transmembrane ion exchange mechanisms, especially voltage-gated potassium and cation transporters. All spatial correlation p -values in **a-c** are adjusted for spatial autocorrelation (see Methods; asterisks in **b,d** indicate $p < 0.05$, 0.01 , 0.005 , and 0.001 respectively; filled circles in **c,d** indicate $p < 0.05$).

Timescales shift in behavior and aging

Finally, we investigate whether timescales are functionally dynamic and relevant for human cognition. While previous studies have shown hierarchical segregation of task-relevant information corresponding to intrinsic timescales of different cortical regions^{15,18,28,29,31,50}, as well as optimal adaptation of behavioral timescales to match the environment^{51,52}, evidence for functionally relevant changes in regional neuronal timescales is lacking. Here, we examine whether timescales undergo short- and long-term shifts during working memory maintenance and aging, respectively.

We first analyze human ECoG recordings where participants performed a visuospatial working memory task that requires a delayed cued response (Fig. 4a)⁵³. Neuronal timescales were extracted for pre-stimulus baseline and memory maintenance delay periods (900 ms, both stimulus-free). Replicating our previous result, we observe that baseline neuronal timescales follow a hierarchical progression across association regions (Fig. 4b). If neuronal timescales track the temporal persistence of information in a functional manner, then they should expand during delay periods. Consistent with our prediction, timescales in all regions are ~20% longer during delay periods (Fig. 4c; $p < 0.005$ for all regions). Moreover, timescale changes in the PFC are significantly correlated with behavior across participants, where longer delay-period timescales relative to baseline are associated with better working memory performance ($\rho = 0.75$, $p = 0.003$). No other spectral features in the recorded brain regions experience consistent changes from baseline to delay periods while also significantly correlating with individual performance, including the $1/f$ -like spectral exponent, narrowband theta (3-8 Hz), and high-frequency (high gamma; 70-100 Hz) activity power (Extended Data Fig. 7).

In the long-term, aging is associated with a broad range of functional and structural changes, such as working memory impairments^{54,55}, as well as changes in neuronal dynamics⁵⁴⁻⁵⁶ and cortical structure^{57,58}, such as the loss of slow-deactivating NMDA receptor subunits⁵⁸. Since neuronal timescales support working memory maintenance, we specifically predict that timescales shorten across the lifespan, in agreement with the observed cognitive and structural deteriorations. To this end, we leverage the wide age range in the MNI-iEEG dataset (13-62 years old) and probe cortical timescales for each participant as a function of age. We observe that older adults have faster neuronal timescales ($\rho = -0.31$, $p = 0.010$; Fig. 3e and Extended Data Fig. 7; see Methods), and that timescales shorten with age in most areas across the cortex ($t = -7.04$, $p < 0.001$). This timescale compression is especially prominent in sensorimotor, temporal, and medial frontal regions (Fig. 3f and Extended Data Fig. 7). These results support our hypothesis that neuronal timescales, estimated from transmembrane current fluctuations, can rapidly shift in a functionally relevant manner, as well as slowly—over decades—in healthy aging.

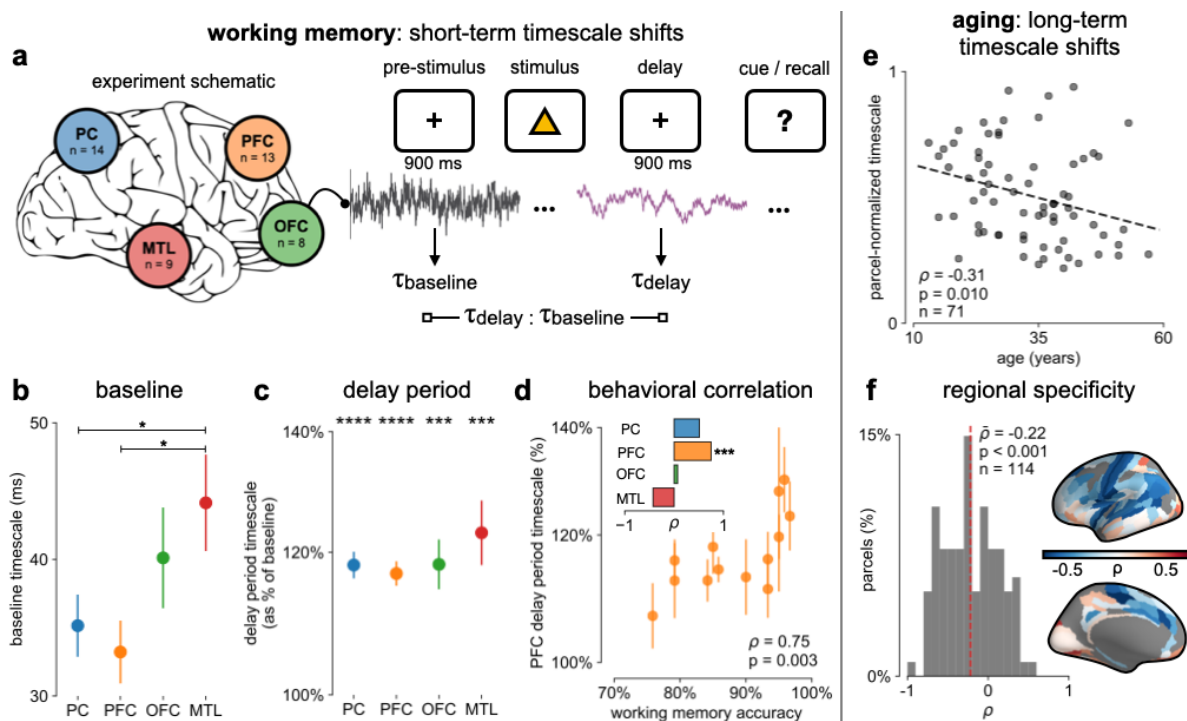


Fig. 4| Timescales expand during working memory maintenance while tracking performance, and task-free average timescales compress in older adults. **a**, 14 participants with overlapping intracranial coverage performed a visuospatial working memory task, with baseline (pre-stimulus) and delay period data analyzed (PC: parietal, PFC: prefrontal, OFC: orbitofrontal, MTL: medial temporal; n denotes number of subjects). **b**, baseline timescales follow hierarchical organization within association regions (*: $p < 0.05$; mean \pm s.e.m. across participants). **c**, all regions show significant timescale increase during delay period compared to baseline (***: $p < 0.005$, ****: $p < 0.001$, one-sample t-test). **d**, PFC timescale expansion during delay periods predicts working memory accuracy across participants (mean \pm s.e.m. across PFC electrodes); inset: correlation between working memory accuracy and timescale change across regions. **e**, in the MNI-iEEG dataset, participant-average cortical timescales decrease (become faster) with age. **f**, most cortical parcels show a negative relationship between timescales and age, with the exception of parts of the visual cortex and the temporal poles (one-sample t-test, $t = -7.04$).

Discussion

Theoretical accounts and converging empirical evidence predict a graded variation of neuronal timescales across the human cortex^{2,4,8}, which reflects functional specialization and implements hierarchical temporal processing crucial for complex cognition¹. This timescale gradient is thought to emerge as a consequence of cortical variations in cytoarchitecture and microcircuit connectivity, thus linking brain structure to function. In this work, we infer the timescale of non-rhythmic transmembrane current fluctuations from invasive human intracranial recordings and test those predictions explicitly.

We find that neuronal timescales vary continuously across the human cortex and coincide with the anatomical hierarchy, with timescales increasing from primary sensory and motor to association regions. Timescales inferred from macaque ECoG scale with single-unit spiking timescales, corroborating the fact that field potential signals mainly reflect fast transmembrane and synaptic currents³³, whose timescales are related to, but distinct from, single-unit timescales measured in previous studies^{10,14,28}. Because field potential fluctuations are driven by currents from both locally generated and distal inputs, our results raise questions on how and when these timescales interact to shape downstream spiking dynamics.

Furthermore, transcriptomic analysis demonstrates the specific roles that transmembrane ion transporters and synaptic receptors play in establishing the cortical gradient of neuronal timescales, over and above the degree predicted by the principal structural gradient alone. The expression of voltage-gated potassium channel, chloride channel, and GABAergic receptor genes, in particular, are strongly associated with the spatial variation of neuronal timescale. Remarkably, we find that electrophysiology/transcriptomic relationships discovered at the single-cell level, through patch-clamp recordings and single-cell RNA sequencing, are recapitulated at the macroscale between bulk gene expression and timescales inferred from ECoG. Our findings motivate further studies for investigating the precise roles voltage-gated ion channels and synaptic inhibition play in shaping functional neuronal timescales through causal manipulations, complementary to existing lines of research focusing on NMDA activation and recurrent circuit motifs.

Finally, we show that neuronal timescales are not static, but can change both in the short- and long-term. Transmembrane current timescales across multiple association regions, including parietal, frontal, and medial temporal cortices, increase during the delay period of a working memory task, consistent with the emergence of persistent spiking during working memory delay. Working memory performance across individuals, however, is predicted by the extent of timescale increase in the PFC only. This further suggests that behavior-relevant neural activity may be localized despite widespread task-related modulation⁵⁹, even at the level of neuronal membrane fluctuations. In the long-term, we find that neuronal timescale shortens with age in most cortical regions, linking age-related synaptic, cellular, and connectivity changes—particularly those that influence neuronal integration timescale—to the compensatory posterior-to-anterior shift of functional specialization in healthy aging²⁷.

Overall, we identify consistent and converging patterns between transcriptomics, anatomy, dynamics, and function across multiple datasets of different modalities from different individuals and multiple species. As a result, evidence for these relationships can be supplemented by more targeted approaches such as imaging of receptor metabolism. Furthermore, the introduction and validation of a novel method for inferring timescales from macroscale electrophysiological recordings potentially allows for the non-invasive estimation of neuronal timescales, using widely accessible tools such as EEG and MEG⁴⁵. These results open up many avenues of research for discovering potential relationships between microscale gene expression and anatomy with the dynamics of neuronal population activity at the macroscale in humans.

Methods

Inferring timescale from autocorrelation and power spectral density

Consistent with previous studies, we define “neuronal timescale” as the exponential decay time constant (τ) of the empirical autocorrelation function (ACF), or lagged correlation^{10,29}. τ can be naively estimated to be the time it takes for the ACF to decrease by a factor of e when there are no additional long-term, scale-free, or oscillatory processes, or by fitting a function of the form $f(t) = e^{-\frac{t}{\tau}}$ and extracting the parameter τ . Equivalently, the power spectral density (PSD) is the Fourier Transform of the ACF via Wiener-Khinchin theorem, and follows a Lorentzian function of the form $L(f) = \frac{A}{k + f^\chi}$ for approximately exponential-decay processes, with $\chi = 2$ exactly when the ACF is solely composed of an exponential decay term, though it is often variable and in the range between 2-6 for neural time series^{34,54,60,61}. Timescale can be computed from the parameter k as $\tau = \frac{1}{2\pi f_k}$, where $f_k \approx k^{1/\chi}$ is approximated to be the frequency at which a bend or knee in the power spectrum occurs and equality holds when $\chi = 2$.

Computing power spectral density (PSD)

PSDs are estimated using a modified Welch’s method, where short-time windowed Fourier transforms (STFT) are computed from the time series, but the median is taken across time instead of the mean (in conventional Welch’s method) to minimize the effect of high-amplitude transients and artifacts⁶². Custom functions for this can be found in NeuroDSP⁶³, a published and open-source digital signal processing toolbox for neural time series (`neurodsp.spectral.compute_spectrum`). For simulated data, Neurotycho macaque ECoG, and MNI-iEEG datasets, we use 1-second long Hamming windows with 0.5-s overlap. To estimate single-trial PSDs for the working memory ECoG dataset (Johnson-ECoG^{53,64}), we simply apply Hamming window to 900-ms long epoched time series and compute the squared magnitude of the windowed-Fourier transform.

Spectral parametrization - Fitting Oscillations and 1/f (FOOOF)

We apply spectral parameterization³⁴ to extract timescales from PSDs. Briefly, we decompose log-power spectra into a summation of narrowband periodic components—modeled as Gaussians—and an aperiodic component—modeled as a generalized Lorentzian function centered at 0 Hz ($L(f)$ above). For inferring decay timescale, this formalism can be practically advantageous when a strong oscillatory or variable power-law (χ) component is present, as is often the case for neural signals. While oscillatory and power-law components can corrupt naive measurements of τ as time for the ACF to reach $1/e$, they can be easily accounted for and ignored in the frequency domain as narrowband peaks and $1/f$ -exponent fit. We discard the periodic components and infer timescale from the aperiodic component of the PSD. For a complete mathematical description of the model, see ref³⁴.

Simulation and validation

We simulate the aperiodic background component of neural field potential recordings as autocorrelated stochastic processes by convolving Poisson population spikes with exponentially-decaying synaptic kernels with predefined decay time constants (neurodsp.sim.sim_synaptic_current). PSDs of the simulated data are computed and parameterized as described above, and we compare the fitted timescales with their ground-truth values.

Macaque ECoG and single unit timescales data

Macaque single-unit timescales are taken directly from values reported in Fig. 1c of ref¹⁰. Whole-brain surface ECoG data (1000Hz sampling rate) is taken from the Neurotycho repository^{65,66}, with 8 sessions of 128-channel recordings from two animals (George and Chibi, 4 sessions each). Results reported in Fig. 2 are from ~10 minutes eyes-open resting periods to match the pre-stimulus baseline condition of single-unit experiments. Timescales for individual ECoG channels are extracted and averaged over regions corresponding to single-unit recording areas from¹⁰ (overlaid on top of the ECoG grid locations from one animal in Fig. 2c), which are selected visually based on the overlapping cortical map and landmark sulci/gyri. Each region included between 2-4 electrodes (refer to Extended Data Table 3 for selected ECoG channel indices for each region).

Statistical analysis for macaque ECoG and spiking timescale

For each individual recording session, as well as the grand average, Spearman rank correlation was computed between spiking and ECoG timescales. Linear regression models were fit using the python package `scipy`⁶⁷ (`scipy.stats.linregress`) and the linear slope was used to compute the scaling coefficient between spiking and ECoG timescales.

Variations in neuronal timescale, T1/T2 ratio, and mRNA expression across human cortex

The following sections describe procedures for generating the average cortical gradient maps for neuronal timescale, MR-derived T1w/T2w ratio, and gene expression from the respective raw datasets. All maps were projected onto the 180 left hemisphere parcels of Human Connectome Project's Multimodal Parcellation⁶⁸ (HCP-MMP1.0) for comparison, described in the individual sections. All spatial correlations are computed as Spearman rank correlations between maps. Procedure for computing statistical significance while accounting for spatial autocorrelation is described in detail below under the sections **spatial statistics** and **spatial autocorrelation modeling**.

Neuronal timescale map

The MNI Open iEEG dataset consists of 1 minute of resting state data across 1772 channels from 106 epilepsy patients (13-62 years old, 58 males and 48 females), recorded using either surface strip/grid or stereoEEG electrodes, and cleaned of visible artifacts^{35,69}. Neuronal timescales were extracted from PSDs of individual channels, and projected from MNI voxel coordinates onto HCP-MMP1.0 surface parcellation as follows:

For each patient, timescale estimated from each electrode was extrapolated to the rest of the cortex in MNI coordinates using a Gaussian weighting function (confidence mask), $w(r) =$

$e^{-(r^2/\alpha^2)}$, where r is the Euclidean distance between the electrode and a voxel, and α is the distance scaling constant, chosen here such that a voxel 4mm away has 50% weight (or, confidence). Timescale at each voxel is computed as a weighted spatial average of timescales from all electrodes (i) of that patient,

$$\text{i.e., } \tau_{\text{voxel}} = \frac{\sum_i w(r_i) \tau_i}{\sum_i w(r_i)}.$$

Similarly, each voxel is assigned a confidence rating that is the maximum of weights over all electrodes ($w_{\text{voxel}}(r_{\text{min}})$, of the closest electrode), i.e., a voxel right under an electrode has a confidence of 1, while a voxel 4mm away from the closest electrode has a confidence of 0.5, etc.

Timescales for each HCP-MMP parcel were then computed as the confidence-weighted arithmetic mean across all voxels that fall within the boundaries of that parcel. HCP-MMP boundary map is loaded and used for projection using NiBabel⁷⁰. This results in a 180 parcels-by-106 patients timescale matrix. A per-parcel confidence matrix of the same dimensions was computed by taking the maximum confidence over all voxels for each parcel (Extended Data Fig. 1a). The average cortical timescale map (gradient) is computed by taking the confidence-weighted average at each parcel across all participants. Note that this procedure for locally thresholded and weighted average is different from projection procedures used for the mRNA and T1w/T2w data due to region-constrained and heterogeneous ECoG electrode sites across participants. While coverage is sparse and idiosyncratic in individual participants, it does not vary as a function of age, and when pooling across the entire population, 178 of 180 parcels have at least one patient with an electrode within 4mm, with the best coverage in later sensorimotor, temporal, and frontal regions (Extended Data Fig. 1).

T1w/T2w ratio map

As a measure of structural cortical hierarchy, we used the ratio between T1- and T2-weighted structural MRI, referred to as T1w/T2w map in main text, or the myelin map^{12,23}. Since there is little variation in the myelin map across individuals, we used the group average myelin map of the WU-Minn HCP S1200 release (N = 1096, March 1, 2017 release) provided in HCP-MMP1.0 surface space. For correlation with other variables, we computed the median value per parcel, identical to the procedure for mRNA expression below.

mRNA expression maps

We used the Allen Human Brain Atlas (AHBA) gene expression dataset^{11,71} that comprised postmortem samples of 6 donors (1 female, 5 male) that underwent microarray transcriptional profiling. Spatial maps of mRNA expression were available in volumetric 2 mm isotropic MNI space, following improved nonlinear registration and whole-brain prediction using variogram modeling as implemented by ref¹³. We used whole-brain maps available from ref¹³ rather than the native sample-wise values in the AHBA database to prevent bias that could occur due to spatial inhomogeneity of the sampled locations. In total, 18114 genes were included for analyses that related to the dominant axis of expression across the genome.

We projected the volumetric mRNA expression data onto the HCP-MMP cortical surface using the HCP workbench software (v1.3.1 running on Windows OS 10) with the “enclosing” method, and custom MATLAB code (github.com/rudyvdbrink/surface_projection). The enclosing method extracts for all vertices on the surface the value from enclosing voxels in the volumetric data. Alternative projection methods such as trilinear 3D linear interpolation of surrounding voxels, or ribbon mapping that constructs a polyhedron from each vertex's neighbors on the surface to compute a weighted mean for the respective vertices, yielded comparable values, but less complete cortical coverage. Moreover, the enclosing method ensured that no transformation of the data (non-linear or otherwise) occurred during the projection process and thus the original values in the volumetric data were preserved.

Next, for each parcel of the left hemisphere in HCP-MMP, we extracted the median vertex-wise value. We used the median rather than the mean because it reduced the contribution of outliers in expression values within parcels. Vertices that were not enclosed by voxels that contained data in volumetric space were not included in the parcel-wise median. This was the case for 539 vertices (1.81% of total vertices). Linear interpolation across empty vertices prior to computing median parcel-wise values yielded near-identical results ($r = 0.95$ for reconstructed surfaces). Lastly, expression values were mean and variance normalized across parcels to facilitate visualization. Normalization had no effect on spatial correlation between gene expression and other variables since the spatial distribution of gene expression was left unaltered.

Spatial statistics

All correlations between spatial maps (timescale, T1w/T2w, gene principal component, and individual gene expressions) were computed using Spearman rank correlation. As noted in ref^{12,72,73}, neural variables vary smoothly and continuously across the cortical surface, violating the assumption of independent samples. As a result, when correlating two variables each with non-trivial spatial autocorrelation, the naive p-value is artificially lowered since it is compared against an inappropriate null hypothesis, i.e., randomly distributed or shuffled values across space. Instead, a more appropriate null hypothesis introduces spatial autocorrelation-preserving null maps, which destroys any potential correlation between two maps while respecting their spatial autocorrelations. For all spatial correlation analyses, we generated $N = 1000$ null maps of one variable (timescale map unless otherwise noted), and the test statistic, Spearman correlation (ρ), is computed against the other variable of interest to build the null distribution. Two-tailed significance is then computed as the proportion of the null distribution that is less extreme than the empirical correlation value. All regression lines were computed by fitting a linear regression to log-timescale and the structural feature maps.

Spatial autocorrelation modeling

To generate spatial autocorrelation-preserving null maps, we used Moran's Spectral Randomization (MSR)⁷⁴ from the python package BrainSpace⁷³. Details of the algorithm can be found in the above references. Briefly, MSR performs eigendecomposition on a spatial weight matrix of choice, which is taken here to be the inverse average geodesic distance matrix between all pairs of parcels in HCP-MMP1.0. The eigenvectors of the weight matrix are then

used to generate randomized null feature maps that preserves the autocorrelation of the empirical map. We used the singleton procedure for null map generation. All significance values reported (Fig. 2b, Fig. 4a-c) were adjusted using the above procedure.

We also compare two other methods of generating null maps: spatial variogram fitting⁷² and spin permutation⁷⁵. Null maps were generated for timescale using spatial variogram fitting, while for spin permutation they were generated for vertex-wise T1w/T2w and gene PC1 maps before parcellation, so as to preserve surface locations of the parcellation itself. All methods perform similarly, producing comparable spatial autocorrelation in the null maps, assessed using spatial variogram, as well as null distribution of spatial correlation coefficients between timescale and T1w/T2w (Extended Data Fig. 2).

Principal Component Analysis (PCA) of gene expression

We used scikit-learn⁷⁶ PCA (sklearn.decomposition.PCA) to identify the dominant axes of gene expression variation across the entire AHBA dataset, as well as for brain-specific genes. PCA was computed on the variance-normalized average gene expression maps, X , an $N \times P$ matrix where $N = 18114$ (or $N = 2429$ brain-specific) genes, and $P = 180$ cortical parcels. Briefly, PCA factorizes X such that $X = USV^T$, where U and V are unitary matrices of dimensionality $N \times N$ and $P \times P$, respectively. S is the same dimensionality as X and contains non-negative descending eigenvalues on its main diagonal (Λ). Columns of V are defined as the principal components (PCs), and the dominant axis of gene expression is then defined as the first column of V , whose proportion of variance explained in the data is the first element of Λ divided by the sum over Λ . Results for PC1 and PC2-10 are shown in Fig. 3a and Extended Data Fig. 4, respectively.

Selection of brain-specific genes

Similar to ref^{12,77,78}, $N=2429$ brain-specific genes were selected based on the criteria that expression in brain tissues were 4 times higher than the median expression across all tissue types, using Supplementary Dataset 1 of ref⁷⁸. PC1 result shown in Fig. 3a is computed from brain-specific genes, though findings are identical when using all genes ($\rho = -0.56$ with timescale map, Extended Data Fig. 4).

Comparison of timescale-transcriptomic association with single-cell timescale genes

Single-cell timescale genes were selected based on data from Table S3 and Online Table 1 of refs^{39,44}, respectively. Using single-cell RNA sequencing data and patch-clamp recordings from transgenic mice cortical neurons, these studies identified genes whose expression significantly correlated with electrophysiological features derived from generalized linear integrate and fire (GLIF) model fits. We selected genes that were significantly correlated to membrane time constant (τ), input resistance (R_{in} or r_i), or capacitance (C_m or cap) in the referenced data tables, and extracted the level of association between gene expression and those electrophysiological feature (correlation 'DiscCorr' in ref⁴⁴ and linear coefficient "beta_gene" in ref³⁹).

To compare timescale-gene expression association at the single-cell and macroscale level, we correlated the single-cell associations extracted above with the spatial correlation coefficient (macroscale ρ) between ECoG timescale and AHBA microarray expression data for those same genes, restricting to genes with $p < 0.05$ for macroscale correlation (results identical for non-restrictive gene set). Overall association for all genes, as well as split by quintiles of their absolute macroscale correlation coefficient, are shown in Fig. 3d. Example “single-cell timescale” genes shown in Fig. 3b,c are genes showing the highest correlations with those electrophysiology features reported in Table 2 of ref³⁹.

T1w/T2w-removed timescale and gene expression residual maps

To remove anatomical hierarchy as a potential mediating variable in timescale-gene expression relationships, we linearly regress out the T1w/T2w map from the (log) timescale map and individual gene expression maps. T1w/T2w was linearly fit to log-timescale, and the error between T1w/T2w-predicted timescale and empirical timescale was extracted (residual); this identical procedure was applied to every gene expression map to retrieve the gene residuals. Spatial autocorrelation-preserving null residual maps were similarly created using MSR.

Partial least squares regression model

Due to multicollinearity in the high-dimensional gene expression dataset (many more genes than parcels), we fit a partial least squares model to the timescale map with one output dimension (`sklearn.cross_decomposition.PLSRegression`) to estimate regression coefficient for all genes simultaneously, resulting in $N=18114$ (or $N=2429$ brain-specific) PLS weights^{46,79}. To determine significantly associated (or, “enriched”) genes, we repeated the above PLS-fitting procedure 1000 times but replaced the empirical timescale map (or residual map) with null timescale maps (or residual maps) that preserved its spatial autocorrelation. Genes whose absolute empirical PLS weight that was greater than 95% of its null weight distribution was deemed to be enriched, and submitted for gene ontology enrichment analysis.

Gene ontology enrichment analysis (GOEA)

The Gene Ontology (GO) captures hierarchically structured relationships between GO items representing aspects of biological processes (BP), cellular components (CC), or molecular functions (MF). For example, “synaptic signaling”, “chemical synaptic transmission”, and “glutamatergic synaptic transmission” are GO items with increasing specificity, with smaller subsets of genes associated with each function. Each GO item is annotated with a list of genes that have been linked to that particular process or function. GOEA examines the list of enriched genes from above to identify GO items that are more associated with those genes than expected by chance. We used GOATOOLS⁴⁷ to perform GOEA programmatically in python.

The list of unranked genes with significant empirical PLS weights was submitted for GOEA as the “study set”, while either the full ABHA list or brain-specific gene list was used as the “reference set”. The output of GOEA is a list of GO terms with annotated genes that are enriched or purified (i.e., preferentially appearing or missing in the study list, respectively) more often than by chance, determined by Fisher’s exact test.

Enrichment ratio is defined as follows: given a reference set with N total genes, and n were found to be significantly associated with timescale (in the study set), for a single GO item with B total genes annotated to it, where b of them overlap with the study set, then $enrichment = \frac{b/n}{B/N}$.

Statistical significance is adjusted for multiple comparisons following Benjamini-Hochberg procedure (false discovery rate q -value reported in Fig. 3f), and all significant GO items ($q < 0.05$) are reported in Fig. 3f, in addition to some example items that did not pass significance threshold. For a detailed exposition, see ref⁶⁰. Fig. 3f shows results using brain-specific genes. The GO items that are significantly associated are similar when using the full gene set, but typically with larger q -values (Extended Data Tables 3 and 4) due to a much larger set of (non-brain-specific) genes.

Working memory ECoG data and analysis

The CRCNS fcx-2 and fcx-3 datasets include 17 intracranial ECoG recordings in total from epilepsy patients (10 and 7, respectively) performing the same visuospatial working memory task^{53,64,81,82}. Subject 3 (s3) from fcx-2 was discarded due to poor data quality upon examination of trial-averaged PSDs (high noise floor near 20 Hz), while s5 and s7 from fcx-3 correspond to s5 and s8 in fcx-2 and were thus combined. Together, data from 14 unique participants (22-50 years old, 5 female) were analyzed, with variable and overlapping coverage in parietal cortex (PC, $n=14$), prefrontal cortex (PFC, $n=13$), orbitofrontal cortex (OFC, $n=8$), and medial temporal lobe (MTL, $n=9$). Each channel was annotated as belonging to one of the above macro regions.

Experimental setup is described in ref^{53,64,81,82} in detail. Briefly, following a 1-second pre-trial fixation period (baseline), subjects were instructed to focus on one of two stimulus contexts (“identity” or “relation” information). Then two shapes were presented in sequence for 200 ms each. After a 900 or 1150 ms jittered precue delay (delay1), the test cue appeared for 800 ms, followed by another post-cue delay period of the same length (delay2). Finally, the response period required participants to perform a 2-alternative forced choice test based on the test cue, which varied based on trial condition. For our analysis, we collapsed across the stimulus context conditions and compared neuronal timescales during the last 900 ms of baseline and delay periods from the epoched data, which were free of visual stimuli, in order to avoid stimulus-related event-related potential effects. Behavioral accuracy for each experimental condition was reported for each participant, and we average across both stimulus context conditions to produce a single working memory accuracy per participant.

Single-trial power spectra were computed for each channel as the squared magnitude of the Hamming-windowed Fourier Transform. We used 900 ms of data in all 3 periods (pre-trial, delay1, and delay2). Timescales were estimated by applying spectral parameterization as above, and the two delay-period estimates were averaged to produce a single delay period value. For comparison, we computed single-trial theta (3-8 Hz) and high-frequency activity (high gamma⁸³, 70-100 Hz) powers as the mean log-power within those frequency bins, as well as spectral exponent (χ). Single-trial timescale difference between delay and baseline was calculated as the difference of the log timescales due to the non-normal distribution of single-trial timescale estimates. All other neural features were computed by subtracting baseline from the delay period.

All neural features were then averaged across channels within the same regions, then trials, for each participant, to produce per-participant region-wise estimates, and finally averaged across all participants for the regional average in Fig. 4b,c. one-sample two-sided t-tests were used to determine the statistical significance of timescale change in each region (Fig. 4c), where the null hypothesis was no change between baseline and delay periods (i.e., delay is 100% of baseline). Spearman rank correlation was used to determine the relationship between neural activity (timescale; theta; high-frequency; χ) change and working memory accuracy across participants (Fig. 4d, Extended Data Fig. 6).

Per-subject average cortical timescale across age

Since electrode coverage in the MNI-iEEG dataset is sparse and non-uniform across participants (Extended Data Fig. 1), simply averaging across parcels within individuals to estimate an average cortical timescale per participant confounds the effect of age with the spatial effect of cortical hierarchy. Therefore, we instead first normalize each parcel by its max value across all participants before averaging within participants, excluding those with fewer than 10 valid parcels (71 of 106 subjects remaining; results hold for a range of threshold values; Extended Data Fig. 7b). Spearman rank correlation was used to compute the association between age and average cortical timescale.

Age-timescale association for individual parcels

Each cortical parcel had a variable number of participants with valid timescale estimates above the consistency threshold, so we compute Spearman correlation between age and timescale for each parcel, but including only those with at least 5 participants (114 of 180 parcels, result holds for a range of threshold values; Extended Data Fig. 7c). Spatial effect of age-timescale variation is plotted in Fig. 4f, where parcels that did not meet the threshold criteria are greyed out. Mean age-timescale correlation from individual parcels was significantly negative under one-sample t-test.

References

1. Kiebel, S. J., Daunizeau, J. & Friston, K. J. A hierarchy of time-scales and the brain. *PLoS Comput. Biol.* **4**, e1000209 (2008).
2. Wang, X.-J. Macroscopic gradients of synaptic excitation and inhibition in the neocortex. *Nat. Rev. Neurosci.* (2020) doi:10.1038/s41583-020-0262-x.
3. Duarte, R., Seeholzer, A., Zilles, K. & Morrison, A. Synaptic patterning and the timescales of cortical dynamics. *Curr. Opin. Neurobiol.* **43**, 156–165 (2017).
4. Chaudhuri, R., Knoblauch, K., Gariel, M.-A., Kennedy, H. & Wang, X.-J. A Large-Scale

- Circuit Mechanism for Hierarchical Dynamical Processing in the Primate Cortex. *Neuron* **88**, 419–431 (2015).
5. Duarte, R. & Morrison, A. Leveraging heterogeneity for neural computation with fading memory in layer 2/3 cortical microcircuits. *PLoS Comput. Biol.* **15**, e1006781 (2019).
 6. Gjorgjieva, J., Drion, G. & Marder, E. Computational implications of biophysical diversity and multiple timescales in neurons and synapses for circuit performance. *Curr. Opin. Neurobiol.* **37**, 44–52 (2016).
 7. Hilgetag, C. C. & Goulas, A. ‘Hierarchy’ in the organization of brain networks. *Philos. Trans. R. Soc. Lond. B Biol. Sci.* **375**, 20190319 (2020).
 8. Huntenburg, J. M., Bazin, P.-L. & Margulies, D. S. Large-Scale Gradients in Human Cortical Organization. *Trends Cogn. Sci.* **22**, 21–31 (2018).
 9. Goulas, A., Zilles, K. & Hilgetag, C. C. Cortical Gradients and Laminar Projections in Mammals. *Trends Neurosci.* **41**, 775–788 (2018).
 10. Murray, J. D. *et al.* A hierarchy of intrinsic timescales across primate cortex. *Nat. Neurosci.* **17**, 1661–1663 (2014).
 11. Hawrylycz, M. J. *et al.* An anatomically comprehensive atlas of the adult human brain transcriptome. *Nature* **489**, 391–399 (2012).
 12. Burt, J. B. *et al.* Hierarchy of transcriptomic specialization across human cortex captured by structural neuroimaging topography. *Nat. Neurosci.* **21**, 1251–1259 (2018).
 13. Gryglewski, G. *et al.* Spatial analysis and high resolution mapping of the human whole-brain transcriptome for integrative analysis in neuroimaging. *Neuroimage* **176**, 259–267 (2018).
 14. Ogawa, T. & Komatsu, H. Differential temporal storage capacity in the baseline activity of neurons in macaque frontal eye field and area V4. *J. Neurophysiol.* **103**, 2433–2445 (2010).
 15. Runyan, C. A., Piasini, E., Panzeri, S. & Harvey, C. D. Distinct timescales of population coding across cortex. *Nature* **548**, 92–96 (2017).

16. Zylberberg, J. & Strowbridge, B. W. Mechanisms of Persistent Activity in Cortical Circuits: Possible Neural Substrates for Working Memory. *Annu. Rev. Neurosci.* **40**, 603–627 (2017).
17. Gold, J. I. & Shadlen, M. N. The neural basis of decision making. *Annu. Rev. Neurosci.* **30**, 535–574 (2007).
18. Sarafyazd, M. & Jazayeri, M. Hierarchical reasoning by neural circuits in the frontal cortex. *Science* **364**, (2019).
19. Wimmer, K., Nykamp, D. Q., Constantinidis, C. & Compte, A. Bump attractor dynamics in prefrontal cortex explains behavioral precision in spatial working memory. *Nat. Neurosci.* **17**, 431–439 (2014).
20. Wang, X.-J. Probabilistic decision making by slow reverberation in cortical circuits. *Neuron* **36**, 955–968 (2002).
21. Wang, X. J. Synaptic basis of cortical persistent activity: the importance of NMDA receptors to working memory. *J. Neurosci.* **19**, 9587–9603 (1999).
22. Wang, X.-J. Decision making in recurrent neuronal circuits. *Neuron* **60**, 215–234 (2008).
23. Glasser, M. F. & Van Essen, D. C. Mapping human cortical areas in vivo based on myelin content as revealed by T1- and T2-weighted MRI. *J. Neurosci.* **31**, 11597–11616 (2011).
24. Margulies, D. S. *et al.* Situating the default-mode network along a principal gradient of macroscale cortical organization. *Proc. Natl. Acad. Sci. U. S. A.* **113**, 12574–12579 (2016).
25. Voytek, B. *et al.* Oscillatory dynamics coordinating human frontal networks in support of goal maintenance. *Nat. Neurosci.* **18**, 1318–1324 (2015).
26. Badre, D. & D'Esposito, M. Is the rostro-caudal axis of the frontal lobe hierarchical? *Nat. Rev. Neurosci.* **10**, 659–669 (2009).
27. Davis, S. W., Dennis, N. A., Daselaar, S. M., Fleck, M. S. & Cabeza, R. Que PASA? The posterior--anterior shift in aging. *Cereb. Cortex* **18**, 1201–1209 (2008).
28. Wasmuht, D. F., Spaak, E., Buschman, T. J., Miller, E. K. & Stokes, M. G. Intrinsic neuronal

- dynamics predict distinct functional roles during working memory. *Nat. Commun.* **9**, 3499 (2018).
29. Honey, C. J. *et al.* Slow cortical dynamics and the accumulation of information over long timescales. *Neuron* **76**, 423–434 (2012).
 30. Lerner, Y., Honey, C. J., Silbert, L. J. & Hasson, U. Topographic mapping of a hierarchy of temporal receptive windows using a narrated story. *J. Neurosci.* **31**, 2906–2915 (2011).
 31. Baldassano, C. *et al.* Discovering Event Structure in Continuous Narrative Perception and Memory. *Neuron* **95**, 709–721.e5 (2017).
 32. Watanabe, T., Rees, G. & Masuda, N. Atypical intrinsic neural timescale in autism. *Elife* **8**, (2019).
 33. Buzsáki, G., Anastassiou, C. A. & Koch, C. The origin of extracellular fields and currents-- EEG, ECoG, LFP and spikes. *Nat. Rev. Neurosci.* **13**, 407–420 (2012).
 34. Haller, M. *et al.* Parameterizing neural power spectra. *bioRxiv* 299859 (2018) doi:10.1101/299859.
 35. Frauscher, B. *et al.* Atlas of the normal intracranial electroencephalogram: neurophysiological awake activity in different cortical areas. *Brain* **141**, 1130–1144 (2018).
 36. Koch, C., Rapp, M. & Segev, I. A brief history of time (constants). *Cereb. Cortex* **6**, 93–101 (1996).
 37. van Vugt, B., van Kerkoerle, T., Vartak, D. & Roelfsema, P. R. The Contribution of AMPA and NMDA Receptors to Persistent Firing in the Dorsolateral Prefrontal Cortex in Working Memory. *J. Neurosci.* **40**, 2458–2470 (2020).
 38. Wang, M. *et al.* NMDA receptors subserve persistent neuronal firing during working memory in dorsolateral prefrontal cortex. *Neuron* **77**, 736–749 (2013).
 39. Bomkamp, C. *et al.* Transcriptomic correlates of electrophysiological and morphological diversity within and across excitatory and inhibitory neuron classes. *PLoS Comput. Biol.* **15**, e1007113 (2019).

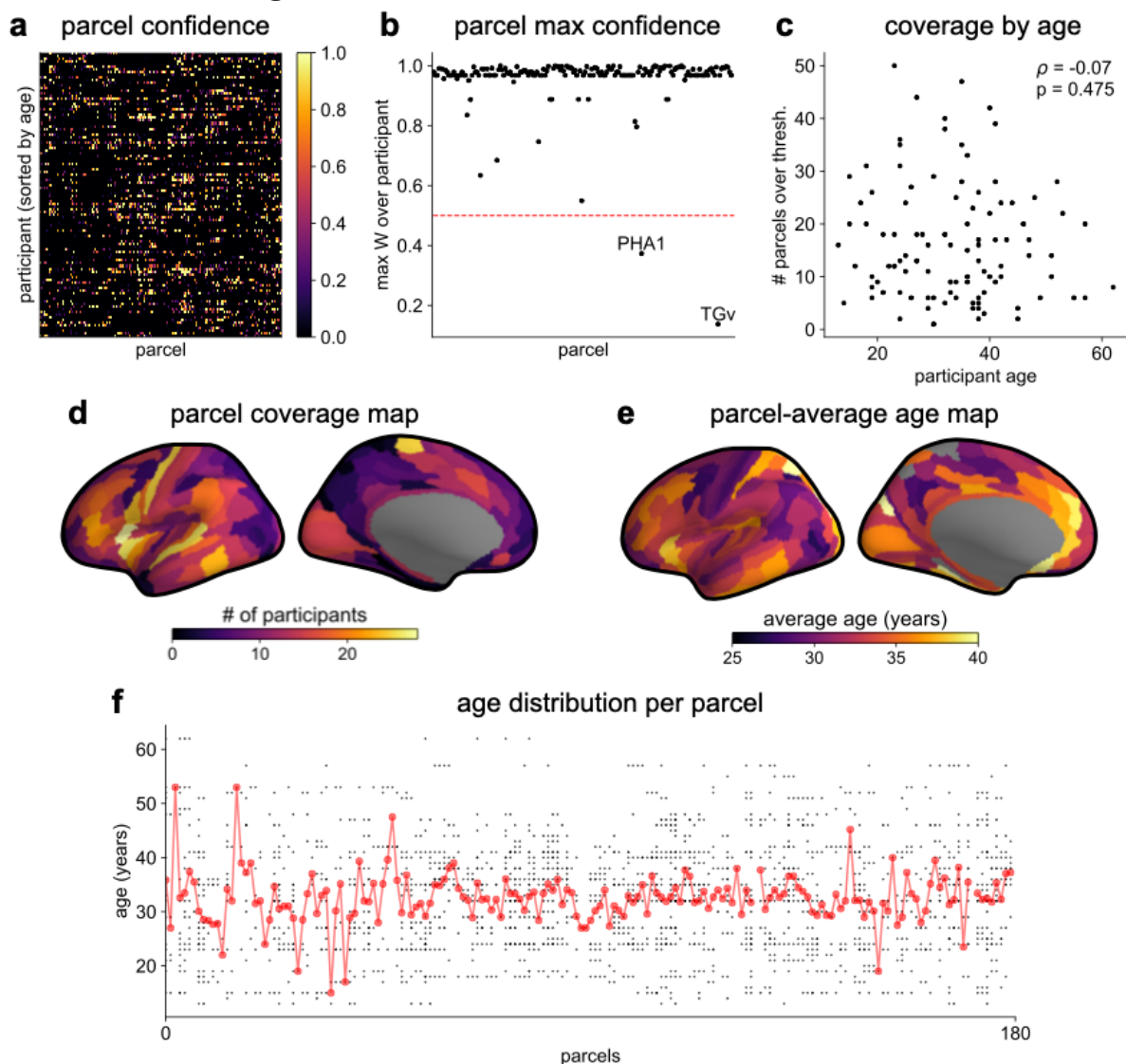
40. Flint, A. C., Maisch, U. S., Weishaupt, J. H., Kriegstein, A. R. & Monyer, H. NR2A subunit expression shortens NMDA receptor synaptic currents in developing neocortex. *J. Neurosci.* **17**, 2469–2476 (1997).
41. Monyer, H., Burnashev, N., Laurie, D. J., Sakmann, B. & Seeburg, P. H. Developmental and regional expression in the rat brain and functional properties of four NMDA receptors. *Neuron* **12**, 529–540 (1994).
42. Eyre, M. D., Renzi, M., Farrant, M. & Nusser, Z. Setting the time course of inhibitory synaptic currents by mixing multiple GABA(A) receptor α subunit isoforms. *J. Neurosci.* **32**, 5853–5867 (2012).
43. Gao, R., Peterson, E. J. & Voytek, B. Inferring synaptic excitation/inhibition balance from field potentials. *Neuroimage* **158**, 70–78 (2017).
44. Tripathy, S. J. *et al.* Transcriptomic correlates of neuron electrophysiological diversity. *PLoS Comput. Biol.* **13**, e1005814 (2017).
45. Demirtaş, M. *et al.* Hierarchical Heterogeneity across Human Cortex Shapes Large-Scale Neural Dynamics. *Neuron* **101**, 1181–1194.e13 (2019).
46. Whitaker, K. J. *et al.* Adolescence is associated with genomically patterned consolidation of the hubs of the human brain connectome. *Proc. Natl. Acad. Sci. U. S. A.* **113**, 9105–9110 (2016).
47. Klopfenstein, D. V. *et al.* GOATOOLS: A Python library for Gene Ontology analyses. *Sci. Rep.* **8**, 10872 (2018).
48. Savaskan, N. E., Bräuer, A. U. & Nitsch, R. Molecular cloning and expression regulation of PRG-3, a new member of the plasticity-related gene family. *Eur. J. Neurosci.* **19**, 212–220 (2004).
49. Telenczuk, B. *et al.* Local field potentials primarily reflect inhibitory neuron activity in human and monkey cortex. *Sci. Rep.* **7**, (2017).
50. Chien, H.-Y. S. & Honey, C. J. Constructing and Forgetting Temporal Context in the Human

- Cerebral Cortex. *Neuron* (2020) doi:10.1016/j.neuron.2020.02.013.
51. Ossmy, O. *et al.* The timescale of perceptual evidence integration can be adapted to the environment. *Curr. Biol.* **23**, 981–986 (2013).
 52. Ganupuru, P., Goldring, A. B., Harun, R. & Hanks, T. D. Flexibility of Timescales of Evidence Evaluation for Decision Making. *Curr. Biol.* **29**, 2091–2097.e4 (2019).
 53. Johnson, E. L. *et al.* Dynamic frontotemporal systems process space and time in working memory. *PLoS Biol.* **16**, e2004274 (2018).
 54. Voytek, B. *et al.* Age-Related Changes in 1/f Neural Electrophysiological Noise. *J. Neurosci.* **35**, 13257–13265 (2015).
 55. Wang, M. *et al.* Neuronal basis of age-related working memory decline. *Nature* **476**, 210–213 (2011).
 56. Voytek, B. & Knight, R. T. Dynamic network communication as a unifying neural basis for cognition, development, aging, and disease. *Biol. Psychiatry* **77**, 1089–1097 (2015).
 57. de Villers-Sidani, E. *et al.* Recovery of functional and structural age-related changes in the rat primary auditory cortex with operant training. *Proc. Natl. Acad. Sci. U. S. A.* **107**, 13900–13905 (2010).
 58. Pegasiou, C. M. *et al.* Age-Dependent Changes in Synaptic NMDA Receptor Composition in Adult Human Cortical Neurons. *Cereb. Cortex* (2020) doi:10.1093/cercor/bhaa052.
 59. Pinto, L. *et al.* Task-Dependent Changes in the Large-Scale Dynamics and Necessity of Cortical Regions. *Neuron* **104**, 810–824.e9 (2019).
 60. Podvalny, E. *et al.* A unifying principle underlying the extracellular field potential spectral responses in the human cortex. *J. Neurophysiol.* **114**, 505–519 (2015).
 61. Miller, K. J., Sorensen, L. B., Ojemann, J. G. & den Nijs, M. Power-law scaling in the brain surface electric potential. *PLoS Comput. Biol.* **5**, e1000609 (2009).
 62. Izhikevich, L., Gao, R., Peterson, E. & Voytek, B. Measuring the average power of neural oscillations. *bioRxiv* 441626 (2018) doi:10.1101/441626.

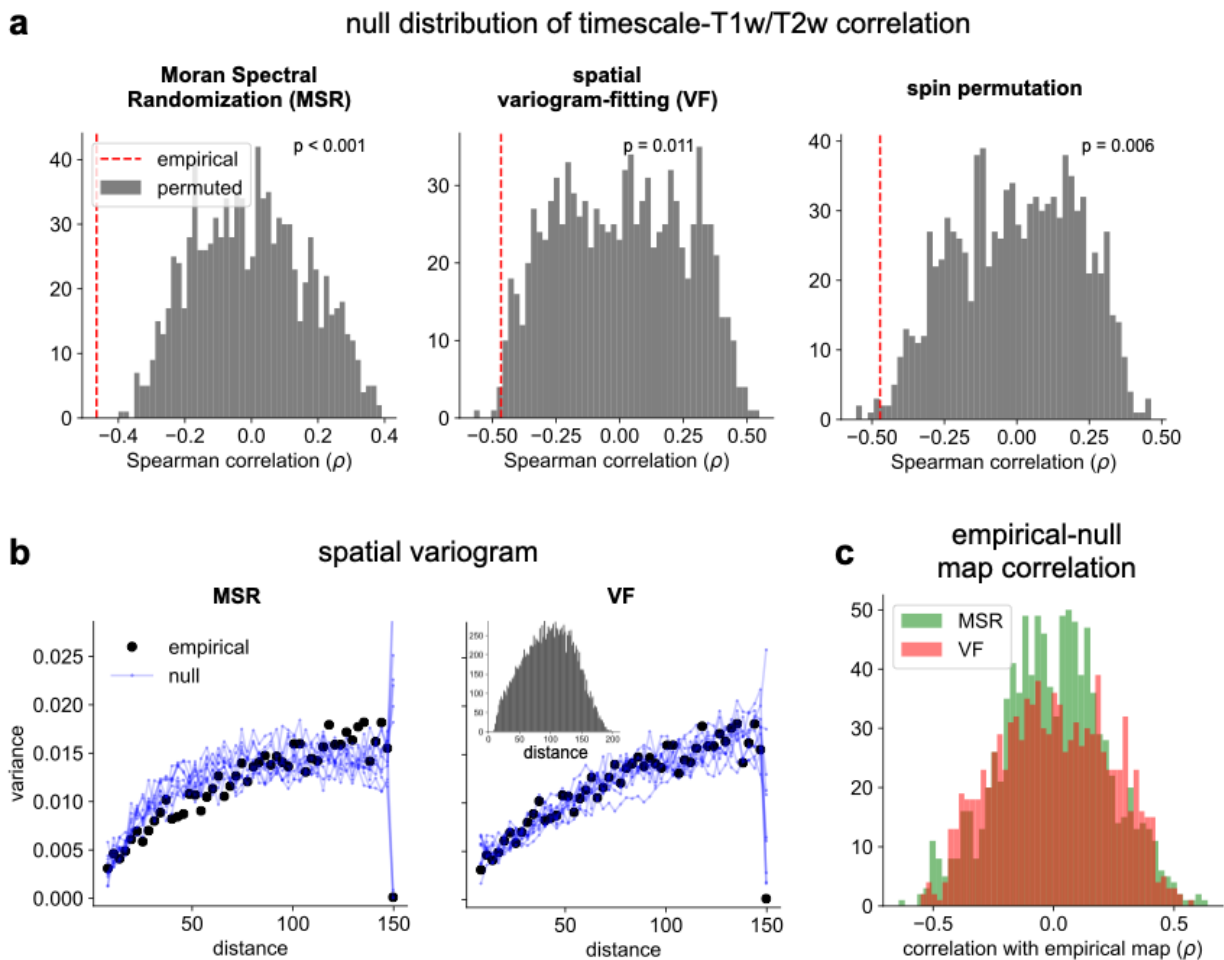
63. Cole, S., Donoghue, T., Gao, R. & Voytek, B. NeuroDSP: a package for neural digital signal processing. *Journal of Open Source Software* **4**, 1272 (2019).
64. Johnson, E. L. *et al.* Spectral Imprints of Working Memory for Everyday Associations in the Frontoparietal Network. *Front. Syst. Neurosci.* **12**, 65 (2018).
65. Nagasaka, Y., Shimoda, K. & Fujii, N. Multidimensional recording (MDR) and data sharing: an ecological open research and educational platform for neuroscience. *PLoS One* **6**, e22561 (2011).
66. Yanagawa, T., Chao, Z. C., Hasegawa, N. & Fujii, N. Large-scale information flow in conscious and unconscious states: an ECoG study in monkeys. *PLoS One* **8**, e80845 (2013).
67. Virtanen, P. *et al.* SciPy 1.0: fundamental algorithms for scientific computing in Python. *Nat. Methods* **17**, 261–272 (2020).
68. Glasser, M. F. *et al.* A multi-modal parcellation of human cerebral cortex. *Nature* **536**, 171–178 (2016).
69. Frauscher, B. *et al.* High-Frequency Oscillations in the Normal Human Brain. *Ann. Neurol.* **84**, 374–385 (2018).
70. Brett, M. *et al.* *nipy/nibabel: 3.1.0.* (2020). doi:10.5281/zenodo.3757992.
71. Hawrylycz, M. *et al.* Canonical genetic signatures of the adult human brain. *Nat. Neurosci.* **18**, 1832–1844 (2015).
72. Burt, J. B., Helmer, M., Shinn, M., Anticevic, A. & Murray, J. D. Generative modeling of brain maps with spatial autocorrelation. *bioRxiv* 2020.02.18.955054 (2020) doi:10.1101/2020.02.18.955054.
73. Vos de Wael, R. *et al.* BrainSpace: a toolbox for the analysis of macroscale gradients in neuroimaging and connectomics datasets. *Commun Biol* **3**, 103 (2020).
74. Wagner, H. H. & Dray, S. Generating spatially constrained null models for irregularly spaced data using Moran spectral randomization methods. *Methods Ecol. Evol.* **6**, 1169–

- 1178 (2015).
75. Alexander-Bloch, A. F. *et al.* On testing for spatial correspondence between maps of human brain structure and function. *Neuroimage* **178**, 540–551 (2018).
 76. Pedregosa, F. Scikit-learn: Machine Learning in Python. *J. Mach. Learn. Res.* **12**, 2825–2830 (2011).
 77. Genovese, G. *et al.* Increased burden of ultra-rare protein-altering variants among 4,877 individuals with schizophrenia. *Nat. Neurosci.* **19**, 1433–1441 (2016).
 78. Fagerberg, L. *et al.* Analysis of the human tissue-specific expression by genome-wide integration of transcriptomics and antibody-based proteomics. *Mol. Cell. Proteomics* **13**, 397–406 (2014).
 79. Vértes, P. E. *et al.* Gene transcription profiles associated with inter-modular hubs and connection distance in human functional magnetic resonance imaging networks. *Philos. Trans. R. Soc. Lond. B Biol. Sci.* **371**, (2016).
 80. Bauer, S. Gene-Category Analysis. in *The Gene Ontology Handbook* (eds. Dessimoz, C. & Škunca, N.) 175–188 (Springer New York, 2017).
 81. Johnson, E. Intracranial EEG recordings of lateral frontal and parietal regions in 7 human adults performing a visuospatial working memory task. (2019) doi:10.6080/K06971S9.
 82. Johnson, E. Intracranial EEG recordings of medial temporal, lateral frontal, and orbitofrontal regions in 10 human adults performing a visuospatial working memory task. (2018) doi:10.6080/K0VX0DQD.
 83. Mukamel, R. *et al.* Coupling between neuronal firing, field potentials, and fMRI in human auditory cortex. *Science* **309**, 951–954 (2005).

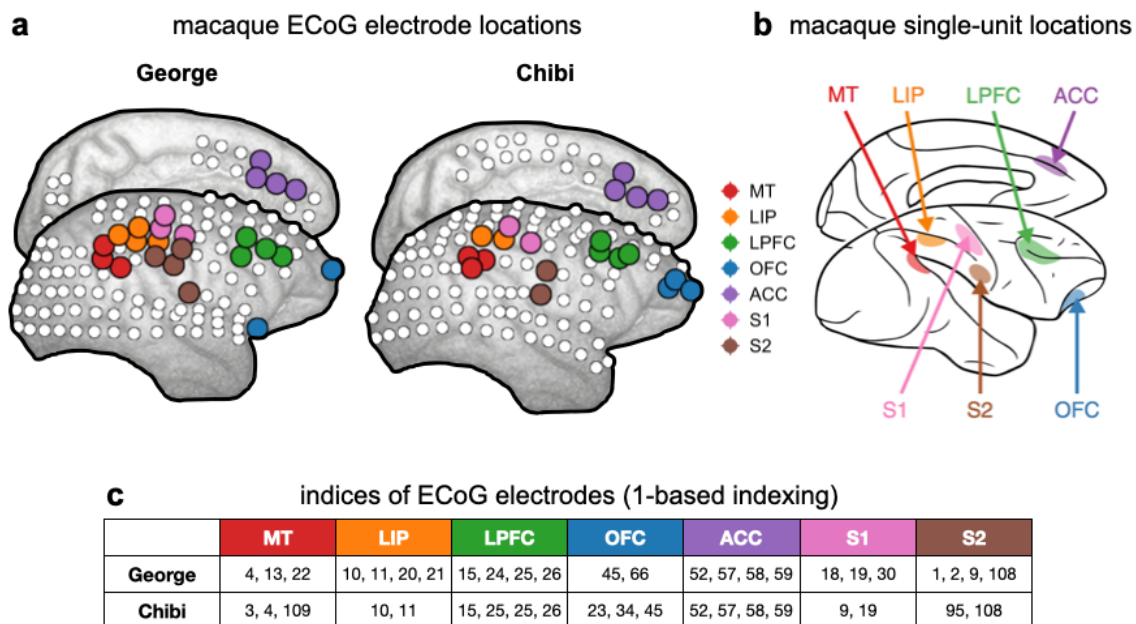
Extended Data Figures and Tables.



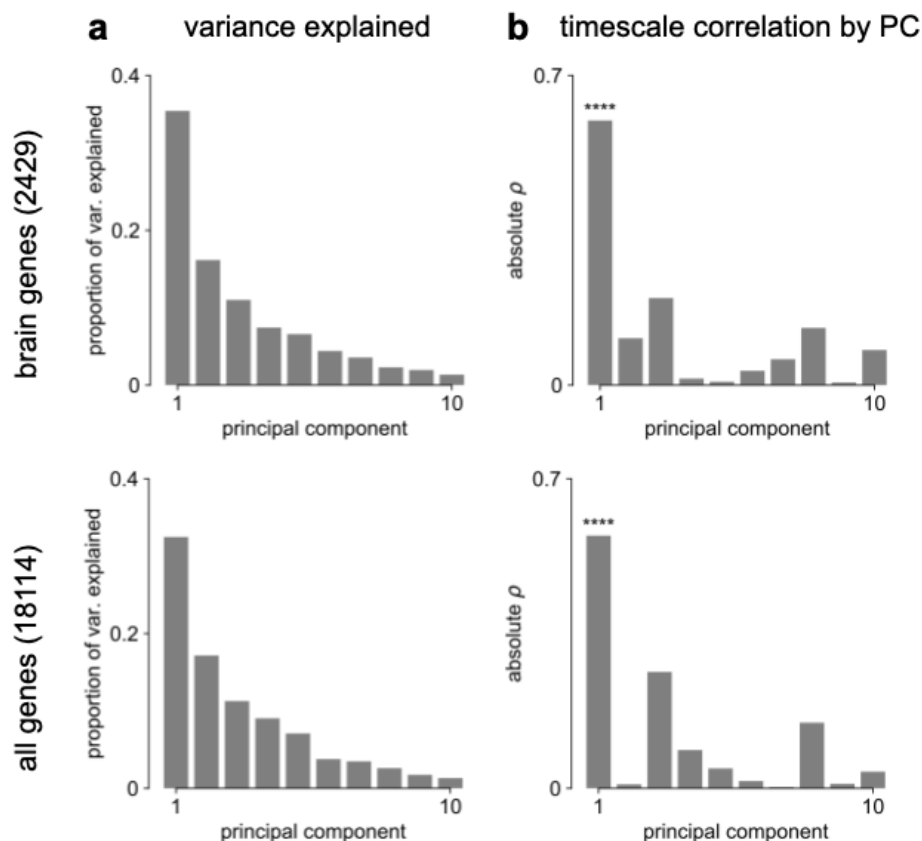
Extended Data Fig. 1 | MNI-iEEG dataset coverage. **a**, per-parcel Gaussian-weighted mask values showing how close the nearest electrode was to a given HCP-MMP1.0 parcel for each participant. Brighter means closer, 0.5 corresponds to the nearest electrode being 4 mm away. **b**, maximum weight for each parcel across all participants. Most parcels have electrodes very close by across the entire participant pool. **c**, the number of HCP-MMP parcels each participant has above the confidence threshold of 0.5 is uncorrelated with age. **d**, number of participants with confidence above threshold at each parcel. Sensorimotor, frontal, and lateral temporal regions have the highest coverage. **e**, average age of participants with confidence above threshold at each parcel. **f**, age distribution of participants with confidence above threshold at each parcel. Average age per parcel (red line) is relatively stable while age distribution varies from parcel to parcel.



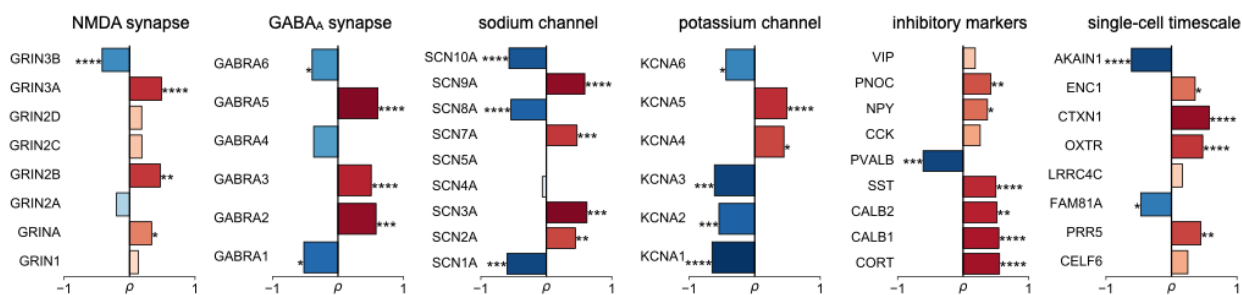
Extended Data Fig. 2 | Comparison of spatial autocorrelation-preserving null map generation methods. **a**, distributions of Spearman correlation values between empirical T1w/T2w map and 1000 spatial-autocorrelation preserving null timescale maps generated using Moran Spectral Randomization (MSR), spatial variogram fitting (VF), and spin permutation. Red dashed line denotes correlation between empirical timescale and T1w/T2w maps, p-values indicate two-tailed significance, i.e., proportion of distribution with values more extreme than empirical correlation. **b**, spatial variogram for empirical timescale map (black) and 10 null maps (blue) generated using MSR and VF. Inset shows distribution of distances between pairs of HCP-MMP parcels. **c**, distribution of Spearman correlations between empirical and 1000 null timescale maps generated using MSR (green) and VF (red), showing similar levels of correlation between empirical and null maps for both methods.



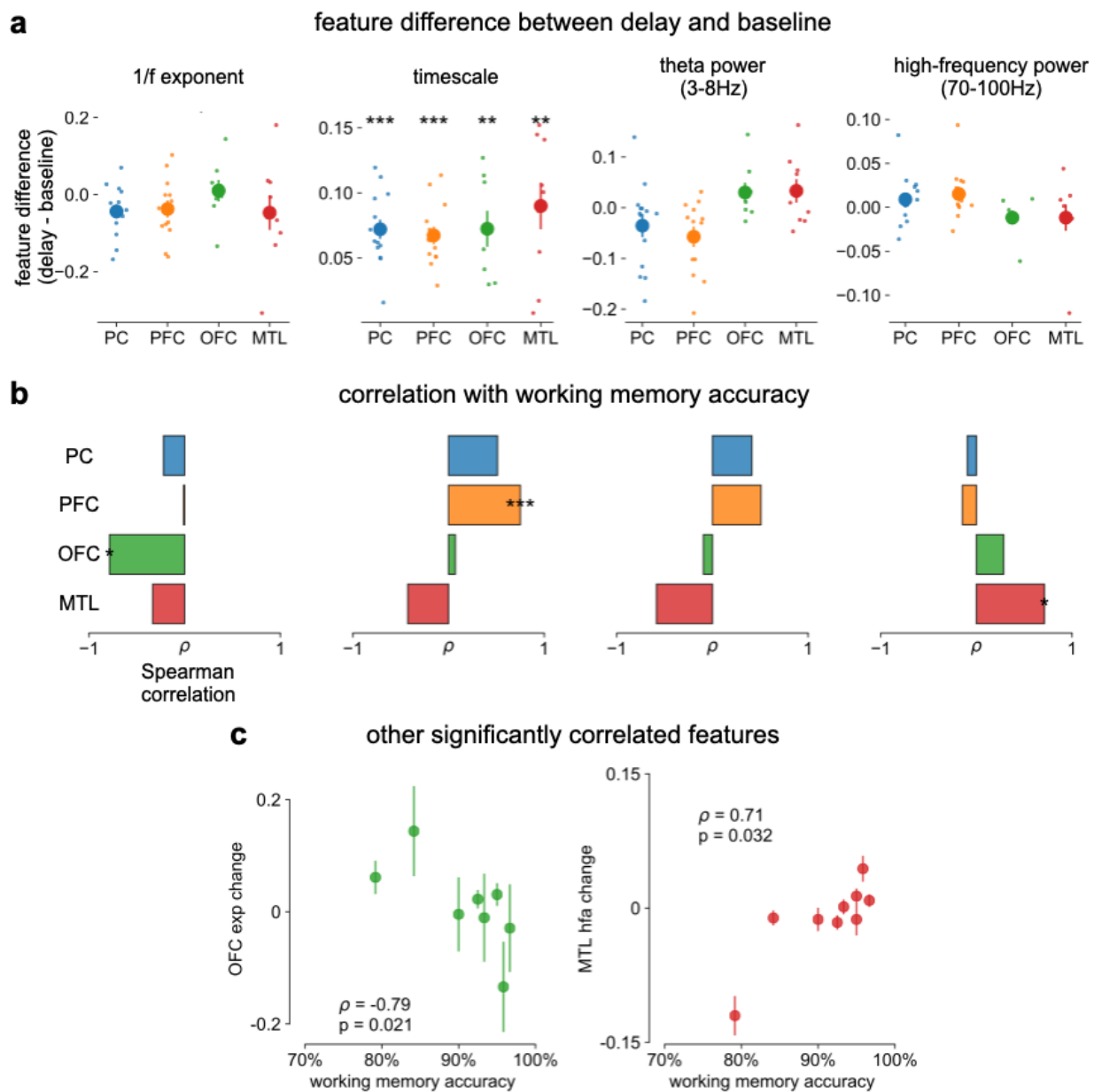
Extended Data Fig. 3| Macaque ECoG and single-unit coverage. **a**, locations of 180-electrode ECoG grid from 2 animals in the Neurotycho dataset, colors correspond to locations used for comparison with single-unit timescales. **b**, single-unit recording locations from Fig. 1a of Murray et al., 2014 (ref¹⁰). **c**, electrode indices of the sampled areas from the two animals, corresponding to those colored in **a**.



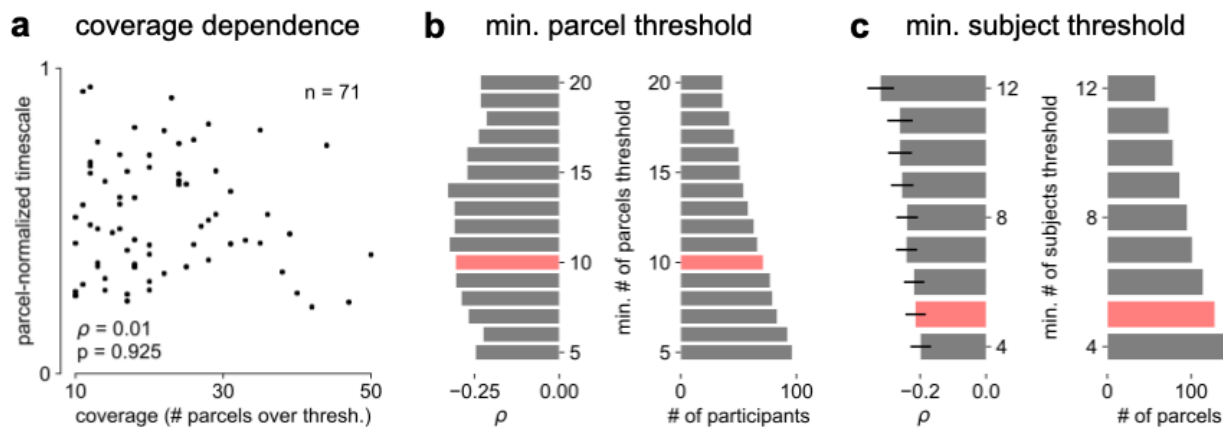
Extended Data Fig. 4 | Transcriptomic PCA results. **a**, proportion of variance explained by the top 10 principal components (PCs) of brain-specific genes (top) and all AHBA genes (bottom). **b**, absolute Spearman correlation between timescale map and top 10 PCs from brain-specific or full gene dataset. Asterisks indicate resampled significance while accounting for spatial autocorrelation, **** indicate $p < 0.001$.



Extended Data Fig. 5 | Individual gene correlations from Fig. 3c with gene symbols labeled, and grouped into functional families.



Extended Data Fig. 6| Spectral correlates of working memory performance. **a**, difference between delay and baseline periods for 1/f-exponent, timescale (same as main Fig. 4c but absolute units on y-axis, instead of percentage), theta power, and high-frequency power. **b**, Spearman correlation between spectral feature difference and working memory accuracy across participants, same features as in **a**. * $p < 0.05$, ** $p < 0.01$, *** $p < 0.005$ in **a** and **b**. **c**, scatter plot of other significantly correlated spectral features from **b**.



Extended Data Fig. 7 | Parameter sensitivity for timescale-aging analysis. a, cortex-averaged timescale is independent of parcel coverage across participants. **b**, sensitivity analysis for the number of valid parcels a participant must have in order to be included in analysis for main Fig. 4e (red). As threshold increases (more stringent), fewer participants satisfy the criteria (right) but correlation between participant age and timescale remains robust (left). **c**, sensitivity analysis for the number of valid participants a parcel must have in order to be included in analysis for main Fig. 4f. As threshold increases (more stringent), fewer parcels satisfy the criteria (right) but average correlation across all parcels remains robust (left, error bars denote s.e.m of distribution as in Fig. 4f).

Extended Data Table 1. Summary of open-access datasets used

Data	Ref.	Specific Source/ Format Used	Relevant Figures
MNI Open iEEG Atlas	35,69		Fig. 2a,b, Fig. 3, Fig. 4e-f
Tw1/T2w map Human Connectome Project	23,68	Release S1200, March 1, 2017	Fig. 2a,b, Fig. 3d-f
Neurotycho macaque ECoG	65,66	Anesthesia datasets, propofol and ketamine (Chibi and Gerge)	Fig. 2c,d
Macaque single-unit timescales	10	Fig. 1 of reference	Fig. 2c,d
Whole-cortex interpolated Allen Brain Atlas human gene expression	11,13	Interpolated maps downloadable from http://www.meduniwien.ac.at/neuroimaging/mRNA.html	Fig. 3
Single-cell timescale-related genes	39,44	Table S3 from ⁴⁴ , Online Table 1 from ³⁹	Fig. 3c,d
Human working memory ECoG	53,64,81,82	CRCNS fcx-2 and fcx-3	Fig. 4a-d

Extended Data Table 2. Reproducing figures from code repository

All IPython notebooks: https://github.com/rdgao/field-echos/tree/master/notebooks	
Notebook	Results
2a_sim_method_schematic.ipynb	simulations: Fig. 1b-e, Extended Data Fig. 3
2b_viz_NeuroTycho-SU.ipynb	macaque timescales: Fig. 2c,d
3_viz_human_structural.ipynb	human timescales vs. T1w/T2w and gene expression: Fig. 2a,b; Fig. 3, Extended Data Fig. 1,4,5 Extended Data Table. 3
4a_viz_human_aging.ipynb	human working memory: Fig. 4e,f, Extended Data Fig. 6
4b_viz_human_wm.ipynb	human aging: Fig. 4a-d, Extended Data Fig. 7
supp_spatialautocorr.ipynb	spatial autocorrelation-preserving nulls: Extended Data Fig. 2
Projection of T1w/T2w and gene expression maps from MNI volumetric coordinates to HCP-MMP1.0 can be found: https://github.com/rudyvdbrink/Surface_projection	

Extended Data Table 3. Significant items from brain-specific GOEA (Fig. 3f)

gene association	ID	e/p	ontology	name	enrichment ratio	p-value (FDR-adjusted)
all	GO:0034702	e	CC	ion channel complex	1.959	0.008
all	GO:1902495	e	CC	transmembrane transporter complex	1.91	0.008
all	GO:1990351	e	CC	transporter complex	1.91	0.008
all	GO:0098982	e	CC	GABA-ergic synapse	2.497	0.038
all	GO:1902711	e	CC	GABA-A receptor complex	4.541	0.038
all	GO:0034707	e	CC	chloride channel complex	3.385	0.038
pos	GO:0008195	e	MF	phosphatidate phosphatase activity	13.864	0.007
neg	GO:0098660	e	BP	inorganic ion transmembrane transport	2.515	0.002
neg	GO:0098662	e	BP	inorganic cation transmembrane transport	2.529	0.007
neg	GO:0098655	e	BP	cation transmembrane transport	2.439	0.007
neg	GO:0034220	e	BP	ion transmembrane transport	2.057	0.03
neg	GO:0030001	e	BP	metal ion transport	2.239	0.036
neg	GO:0071805	e	BP	potassium ion transmembrane transport	3.122	0.036
neg	GO:0006813	e	BP	potassium ion transport	3.081	0.037
neg	GO:1902495	e	CC	transmembrane transporter complex	2.334	0.009
neg	GO:1990351	e	CC	transporter complex	2.334	0.009
neg	GO:0034702	e	CC	ion channel complex	2.36	0.009
neg	GO:0098796	e	CC	membrane protein complex	2.063	0.009
neg	GO:0034703	e	CC	cation channel complex	2.379	0.03
neg	GO:0005244	e	MF	voltage-gated ion channel activity	3.081	0.002
neg	GO:0022832	e	MF	voltage-gated channel activity	3.081	0.002
neg	GO:0046873	e	MF	metal ion transmembrane transporter activity	2.453	0.002
neg	GO:0022890	e	MF	inorganic cation transmembrane transporter activity	2.24	0.005
neg	GO:0005216	e	MF	ion channel activity	2.289	0.006
neg	GO:0008324	e	MF	cation transmembrane transporter activity	2.173	0.006
neg	GO:0015318	e	MF	inorganic molecular entity transmembrane transporter activity	2.04	0.006
neg	GO:0015077	e	MF	monovalent inorganic cation transmembrane transporter activity	2.535	0.006
neg	GO:0015075	e	MF	ion transmembrane transporter activity	2.024	0.006

neg	GO:0015079	e	MF	potassium ion transmembrane transporter activity	3.041	0.006
neg	GO:0005215	e	MF	transporter activity	1.883	0.006
neg	GO:0022857	e	MF	transmembrane transporter activity	1.906	0.006
neg	GO:0022836	e	MF	gated channel activity	2.301	0.006
neg	GO:0015267	e	MF	channel activity	2.191	0.006
neg	GO:0022803	e	MF	passive transmembrane transporter activity	2.191	0.006
neg	GO:0005249	e	MF	voltage-gated potassium channel activity	3.658	0.006
neg	GO:0005261	e	MF	cation channel activity	2.353	0.009
neg	GO:0005267	e	MF	potassium channel activity	3.058	0.011
neg	GO:0022843	e	MF	voltage-gated cation channel activity	2.744	0.022

e/p: enriched or purified; BP: biological process; CC: cellular components; MF: molecular function

Extended Data Table 4. Significant items from all-gene GOEA

gene association	ID	e/p	ontology	name	enrichment ratio	p-value (FDR-adjusted)
all	GO:0034702	e	CC	ion channel complex	1.83	0.008
all	GO:1990351	e	CC	transporter complex	1.774	0.008
all	GO:1902495	e	CC	transmembrane transporter complex	1.79	0.008
all	GO:0034703	e	CC	cation channel complex	1.952	0.009
all	GO:0098982	e	CC	GABA-ergic synapse	2.468	0.048
all	GO:1902711	e	CC	GABA-A receptor complex	5.035	0.048
pos	GO:0050866	e	BP	negative regulation of cell activation	3.596	0
pos	GO:0002376	e	BP	immune system process	1.629	0
pos	GO:0006955	e	BP	immune response	1.992	0
pos	GO:0002695	e	BP	negative regulation of leukocyte activation	3.343	0.001
pos	GO:0045087	e	BP	innate immune response	2.297	0.005
pos	GO:0050865	e	BP	regulation of cell activation	2.099	0.005
pos	GO:0045321	e	BP	leukocyte activation	1.834	0.006
pos	GO:0007165	e	BP	signal transduction	1.301	0.006
pos	GO:0051250	e	BP	negative regulation of lymphocyte activation	3.305	0.007
pos	GO:0070663	e	BP	regulation of leukocyte proliferation	2.82	0.007
pos	GO:0002252	e	BP	immune effector process	1.778	0.009
pos	GO:0050670	e	BP	regulation of lymphocyte proliferation	2.823	0.009
pos	GO:0032944	e	BP	regulation of mononuclear cell proliferation	2.807	0.009
pos	GO:0050776	e	BP	regulation of immune response	1.787	0.011
pos	GO:0002682	e	BP	regulation of immune system process	1.571	0.015
pos	GO:0046634	e	BP	regulation of alpha-beta T cell activation	3.772	0.016
pos	GO:0001775	e	BP	cell activation	1.709	0.016
pos	GO:0032956	e	BP	regulation of actin cytoskeleton organization	2.229	0.016
pos	GO:0003150	e	BP	muscular septum morphogenesis	17.672	0.016
pos	GO:0032945	e	BP	negative regulation of mononuclear cell proliferation	4.208	0.016
pos	GO:0050672	e	BP	negative regulation of lymphocyte proliferation	4.208	0.016
pos	GO:0006952	e	BP	defense response	1.686	0.016

pos	GO:0002694	e	BP	regulation of leukocyte activation	2.013	0.016
pos	GO:0002253	e	BP	activation of immune response	2.183	0.016
pos	GO:0030833	e	BP	regulation of actin filament polymerization	2.832	0.016
pos	GO:0032970	e	BP	regulation of actin filament-based process	2.136	0.017
pos	GO:0002684	e	BP	positive regulation of immune system process	1.708	0.017
pos	GO:0046640	e	BP	regulation of alpha-beta T cell proliferation	6.094	0.017
pos	GO:0050868	e	BP	negative regulation of T cell activation	3.381	0.017
pos	GO:0002274	e	BP	myeloid leukocyte activation	1.926	0.017
pos	GO:0008064	e	BP	regulation of actin polymerization or depolymerization	2.697	0.017
pos	GO:0030832	e	BP	regulation of actin filament length	2.681	0.017
pos	GO:0006334	e	BP	nucleosome assembly	3.053	0.018
pos	GO:0070664	e	BP	negative regulation of leukocyte proliferation	3.956	0.018
pos	GO:0038096	e	BP	Fc-gamma receptor signaling pathway involved in phagocytosis	3.787	0.026
pos	GO:0002433	e	BP	immune response-regulating cell surface receptor signaling pathway involved in phagocytosis	3.787	0.026
pos	GO:0098883	e	BP	synapse pruning	10.041	0.027
pos	GO:0038094	e	BP	Fc-gamma receptor signaling pathway	3.734	0.029
pos	GO:0051249	e	BP	regulation of lymphocyte activation	2.035	0.029
pos	GO:0002431	e	BP	Fc receptor mediated stimulatory signaling pathway	3.682	0.03
pos	GO:0042116	e	BP	macrophage activation	4.734	0.03
pos	GO:0110053	e	BP	regulation of actin filament organization	2.279	0.03
pos	GO:0150064	e	BP	vertebrate eye-specific patterning	22.09	0.03
pos	GO:0002683	e	BP	negative regulation of immune system process	2.008	0.03
pos	GO:0051049	e	BP	regulation of transport	1.428	0.03
pos	GO:0098542	e	BP	defense response to other organism	1.811	0.033
pos	GO:0150146	e	BP	cell junction disassembly	9.204	0.033
pos	GO:0016322	e	BP	neuron remodeling	9.204	0.033
pos	GO:1903038	e	BP	negative regulation of leukocyte cell-cell adhesion	3.04	0.033

pos	GO:0007166	e	BP	cell surface receptor signaling pathway	1.391	0.034
pos	GO:0034728	e	BP	nucleosome organization	2.591	0.037
pos	GO:0036336	e	BP	dendritic cell migration	6.976	0.037
pos	GO:0048584	e	BP	positive regulation of response to stimulus	1.379	0.039
pos	GO:0001774	e	BP	microglial cell activation	5.727	0.039
pos	GO:0002269	e	BP	leukocyte activation involved in inflammatory response	5.727	0.039
pos	GO:0050778	e	BP	positive regulation of immune response	1.82	0.039
pos	GO:2000112	p	BP	regulation of cellular macromolecule biosynthetic process	0.718	0.017
pos	GO:0051252	p	BP	regulation of RNA metabolic process	0.718	0.019
pos	GO:0044271	p	BP	cellular nitrogen compound biosynthetic process	0.554	0.029
pos	GO:0019219	p	BP	regulation of nucleobase-containing compound metabolic process	0.737	0.029
pos	GO:0090304	p	BP	nucleic acid metabolic process	0.654	0.037
pos	GO:0032993	e	CC	protein-DNA complex	2.829	0.016
pos	GO:0000786	e	CC	nucleosome	3.488	0.016
pos	GO:0005887	e	CC	integral component of plasma membrane	1.555	0.016
pos	GO:0031226	e	CC	intrinsic component of plasma membrane	1.536	0.016
pos	GO:0044815	e	CC	DNA packaging complex	3.217	0.023
pos	GO:0030666	e	CC	endocytic vesicle membrane	2.705	0.034
pos	GO:0031514	e	CC	motile cilium	2.897	0.034
pos	GO:0043235	e	CC	receptor complex	1.981	0.04
pos	GO:0000839	e	CC	Hrd1p ubiquitin ligase ERAD-L complex	11.045	0.047
pos	GO:0016021	e	CC	integral component of membrane	1.232	0.047
pos	GO:0005634	p	CC	nucleus	0.79	0.04
pos	GO:0003676	p	MF	nucleic acid binding	0.694	0.012
neg	GO:0006813	e	BP	potassium ion transport	2.911	0.004
neg	GO:0071805	e	BP	potassium ion transmembrane transport	2.868	0.008
neg	GO:0015079	e	MF	potassium ion transmembrane transporter activity	2.888	0.001
neg	GO:0015075	e	MF	ion transmembrane transporter activity	1.726	0.001
neg	GO:0022857	e	MF	transmembrane transporter activity	1.649	0.001

neg	GO:0046873	e	MF	metal ion transmembrane transporter activity	2.068	0.001
neg	GO:0005215	e	MF	transporter activity	1.587	0.002
neg	GO:0022832	e	MF	voltage-gated channel activity	2.468	0.006
neg	GO:0005244	e	MF	voltage-gated ion channel activity	2.468	0.006
neg	GO:0015318	e	MF	inorganic molecular entity transmembrane transporter activity	1.662	0.008
neg	GO:0001227	e	MF	DNA-binding transcription repressor activity, RNA polymerase II-specific	2.227	0.011
neg	GO:0001217	e	MF	DNA-binding transcription repressor activity	2.218	0.011
neg	GO:0022836	e	MF	gated channel activity	2.007	0.015
neg	GO:0005249	e	MF	voltage-gated potassium channel activity	3.126	0.015
neg	GO:0015077	e	MF	monovalent inorganic cation transmembrane transporter activity	1.916	0.022
neg	GO:0005267	e	MF	potassium channel activity	2.703	0.022
neg	GO:0022890	e	MF	inorganic cation transmembrane transporter activity	1.701	0.033

e/p: enriched or purified; BP: biological process; CC: cellular components; MF: molecular function